Defects in exosome biogenesis are associated with sensorimotor defects in zebrafish *vps4a* mutants

Running title: Sensorimotor defects in zebrafish *vps4a* mutants

Anna Shipman[1], Yan Gao[1], Desheng Liu[2], Shan Sun[2], Jingjing Zang[3], Zoha Syed[1], Amol Bhagavathi[1], Eliot Smith[1,4], Timothy Erickson[5], Matthew Hill[1,6], Stephan Neuhauss[3], Sen-Fan Sui[2], Teresa Nicolson[1]

[1]Department of Otolaryngology, Stanford University, Stanford, CA, United States
[2]State Key Laboratory of Membrane Biology, Beijing Frontier Research Center for Biological Structure, Beijing Advanced Innovation Center for Structural Biology, School of Life Sciences, Tsinghua University, Beijing, China
[3]Department of Molecular Life Sciences, University of Zurich, Zurich, Switzerland
[4]Present address: Biotechne Corporation, Newark, CA United States 94304
[5]Department of Biology, University of New Brunswick, Fredericton, Canada
[6]Present address: Department of Otolaryngology, University of Colorado, Aurora, CO, United States

Corresponding author: Teresa Nicolson
Email: tnicolso@stanford.edu

Conflict of Interest Statement: The authors declare no competing financial interests.

Abstract

Mutations in human *VPS4A* are associated with neurodevelopmental defects, including motor delays and defective muscle tone. *VPS4A* encodes a AAA-ATPase that is required for membrane scission, but how mutations in *VPS4A* lead to impaired control of motor function is not known. Here we identified a mutation in zebrafish *vps4a*, T248I, that affects sensorimotor transformation. In biochemical experiments we show that the T248I mutation reduces the ATPase activity of Vps4a and disassembly of its substrate, ESCRT filaments, which mediate membrane scission. Consistent with the established role for Vps4a in the endocytic pathway and exosome biogenesis, *vps4a*^{T248I} mutants have enlarged endosomal compartments in the CNS and decreased numbers of circulating exosomes. Resembling the central form of hypotonia in human *VPS4A* patients, motor neurons and muscle cells are unaffected in mutant zebrafish as they react robustly to touch. Unlike somatosensory function, optomotor responses, vestibulospinal (VS), and acoustic startle reflexes are severely impaired in *vps4a*^{T248I} mutants, indicating a greater sensitivity of these circuits to the T248I mutation. ERG recordings indicate that visual ability is largely reduced in the mutants, however, *in vivo* imaging of tone-evoked responses in the inner ear and ascending auditory pathway show comparable activity. Further investigation of central pathways in *vps4a*^{T248I} mutants revealed that sensory cues failed to fully activate neurons in the VS and medial longitudinal fasciculus (MLF) nuclei that directly innervate motor neurons. Our results suggest that a defect in sensorimotor transformation underlies the profound yet selective effects on motor reflexes resulting from the loss of membrane scission mediated by Vps4a.

59 **Introduction**

60 Neurodevelopmental disorders are a collection of conditions that affect central nervous system
61 growth and development and can have a wide variety of associated clinical signs, such as
62 impaired cognition, difficulties in communication, and motor defects. Many neurodevelopmental
63 disorders are the result of genetic mutations and often target molecular pathways that impact
64 protein synthesis, transcriptional or epigenetic regulation or synaptic signaling [1–3]. An early
65 feature that is common to several neurodevelopmental defects is central hypotonia (low muscle
66 tone), however, it remains unclear how the underlying biochemical and sensorimotor
67 mechanisms can result in this feature [4].

68 *De novo* heterozygous missense mutations in human Vacuolar protein sorting-
69 associated protein 4A (*VPS4A*) have been associated with neurodevelopmental disorders
70 characterized by pronounced delays in development, motor skills and speech, and severe
71 intellectual disabilities and visual dysfunction [5]. Symptoms arising from problems with muscle
72 tone such as hypotonia and dystonia are also thought to be central in nature [6]. In addition,
73 mutations in *VPS4A* are associated with Congenital Dyserythropoietic Anemia [7,8]. *VPS4A*
74 encodes a type I AAA-ATPase that was originally identified in yeast. In multicellular organisms,
75 a paralogue, *VPS4B*, is also expressed and both genes are highly conserved from plants to
76 humans [9–12]. VPS4A binds to the ESCRT-III complex to promote dissociation of the complex
77 via ATP hydrolysis, resulting in membrane scission events that are key for proper viral bud
78 release, cytokinesis, neurite severing, plasma membrane repair and multivesicular body
79 formation [13–16]. In animal studies, it has been previously shown that RNAi knockdown of
80 *vps4* in fruit fly larvae results in defective pruning of neurites and knock out of *Vps4a* in mice
81 results in lethality at preweaning stages [17,18]. In line with the known function of VPS4A,
82 fibroblasts from *VPS4A* human patients display defects in endosomal morphology and cell
83 division [5]. How these defects lead to motor system impairment in probands is not fully
84 understood.

85 Here, we identified a missense mutation in zebrafish *vps4a*, T248I, which was
86 generated in a small scale ENU mutagenesis screen for mutants that display auditory/vestibular
87 defects [19]. Zebrafish have become a model for studying human disease due to the genetic
88 conservation with humans, as well as the relatively short development and life cycle compared
89 to mammalian models, and the large number of available genetic tools and behavioral assays.
90 Brain development and structures within the zebrafish CNS use similar signaling pathways and
91 serve similar functions as those in mammals, making them particularly useful for studying
92 neurodevelopmental diseases [20–25].
93 We show that the zebrafish *vps4a* mutants display endosomal abnormalities and
94 reduced numbers of exosomes in the CNS. Both defects are consistent with the induction of
95 stress response genes in mid- and hindbrain regions of *vps4a*^{T248I} mutants. Using *in vivo*
96 calcium imaging, we detected strongly reduced activity in the motor circuits associated with
97 movements evoked by sensory inputs. These findings support a model where the reduced
98 enzymatic activity of Vps4a results in a disruption in late endosome function and exosome
99 release, consequently reducing cellular homeostasis within neural circuits mediating
100 sensorimotor transformation.
101
102
103 **Results**
104 **A missense mutation in *vps4a* reduces ATPase activity and ESCRT-III filament**
105 **disassembly**
106 *raumschiff* mutants were generated from an ENU mutagenesis screen for genes that affect
107 larval auditory and vestibular function [19]. Mutant larvae fail to respond to auditory cues and
108 maintain an upright posture. The mutation is recessive and fully penetrant at 5 days
109 postfertilization (dpf) with lethality occurring around 9-10 dpf. To identify the causative gene of
110 the *raumschiff* phenotype, we used whole-genome sequencing and identified a threonine to

111 isoleucine missense mutation in *vps4a* using SNPTrack [26]. The critical interval for *raumschiff*
112 was also mapped to a region approximately 700 kb (or 1 cM) south of the polymorphic marker
113 z5669, placing the locus at 34.33 Mb on Chromosome 25. *vps4a* is located at 34.93Mb on
114 Chromosome 25, which is within the predicted region for the causative gene. No other
115 polymorphisms were identified by SNPTrack in this region (Fig 1A).
116 Vps4a is a hexameric type I AAA-ATPase member of the ESCRT-III complex, whose
117 role is to promote the dissociation of the ESCRT-III subunits via ATP hydrolysis [11,13,27,28].
118 The threonine to isoleucine mutation (T248I) we identified is present in the AAA ATPase domain
119 in a region that is highly conserved between species (Fig 1B). To determine whether the T248I
120 mutation was comparable to a nonsense allele of *vps4a*, we edited the *vps4a* locus using
121 multiple CRISPR/Cas9 guides [29,30]. In our experiments, multi-guide injections resulted in a
122 G0 phenotype in 16.9% of injected larvae that was indistinguishable from the auditory/vestibular
123 phenotype observed in *vps4a*^{T248I} mutants (400 embryos were injected at < 1 hour past
124 fertilization; of the larvae that survived to 5 dpf, 56/331 larvae showed absence of acoustic
125 startle reflexes and abnormal posture). These results suggest that the T248I mutation is
126 comparable to a null allele of Vps4a. In addition, the *vps4b* paralogue is also ubiquitously
127 expressed [31], therefore we generated *vps4a/vps4b* G0 double mutants using CRISPR-based
128 editing to test whether *vps4b* could compensate for the loss of *vps4a* during development. A
129 previous study using morpholinos against *vps4b* reported a tooth phenotype analogous to
130 human dentin dysplasia I [31]. We observed that embryos injected with multiple CRISPR
131 guides against *vps4b* alone, or *vps4a* and *vps4b* together, developed normally until 3 dpf. The
132 lack of embryonic lethality is presumably due to the presence of maternal RNA during early
133 developmental stages. However, in contrast to the morpholino study, *vps4b* and *vps4a/4b* multi-
134 guide injected larvae exhibited progressive necrosis and by 5 dpf, there was complete lethality
135 (558 embryos were injected with *vps4b* guides; 468 larvae survived to 1 dpf, and 2 survived to 5
136 dpf. 298 embryos were injected with *vps4a/4b* guides; 236 larvae survived to 1 dpf, and 1

137 survived to 5 dpf). Our results suggest that *vps4b* is required for global cellular homeostasis
138 whereas *vps4a* selectively affects the nervous system. A similar effect was reported for the Nsfa
139 and Nsfb AAA-ATPases that mediate vesicle fusion; mutations in zebrafish *nsfa* largely affect
140 the nervous system, while the loss of *nsfb* functions leads to general necrosis at 4 dpf [32–34].
141 Based on the Cryo-EM structure of the yeast Vps4 AAA-ATPase [35], threonine 248 is
142 located at the interface between Vps4a hexamer subunits (Fig 1C). To assess the effect of the
143 isoleucine substitution on ATPase activity, we generated an equivalent mutation, T254I, in the
144 AAA ATPase domain of yeast Vps4. When tested for ATPase activity *in vitro*, $Vps4^{T254I}$ had
145 severely reduced enzymatic activity compared to wild-type Vps4a, although some activity
146 remained ($p < 0.0001$, $n_{WT} = 4$, $n_{vps4(T254I)} = 4$, $t = 47.92$, df = 6) (Fig 1D).
147 To determine whether the residual function of the T254I protein could mediate filament
148 disassembly, we incubated $Vps4^{T254I}$ with the ESCRT-III filaments formed by Vps2, Vps24 and
149 Snf7 *in vitro* and used sedimentation to assess disassembly. In our assay, disassembled
150 ESCRT-III filament proteins are present in the supernatant whereas assembled filaments
151 sediment to the pellet fraction [35]. We observed that wild-type Vps4a completely disassembled
152 the ESCRT-III filaments, with all proteins found in the supernatant (Fig 1E). In contrast, mutant
153 $Vps4^{T254I}$ only partially disassembled the ESCRT filaments (Fig 1E). Using negative stain
154 electron microscopy (EM), assembled ESCRT-III filaments appear as rings or have corkscrew
155 structures (Fig 1F, upper left panel). When incubated with wild-type Vps4, filament structures
156 were absent, indicating full disassembly (Fig 1F, upper right panel). In the presence of $Vps4^{T254I}$,
157 assembled filaments were still detectable albeit there were fewer filaments compared to
158 samples where no Vps4 protein was added (Fig 1F, lower panels). These results show that the
159 T245I mutation at the interface between Vps4a subunits reduces but does not fully abolish the
160 ATPase activity of the protein, and this reduction in activity is reflected in the incomplete
161 disassociation of ESCRT-III filaments.
162

163 **The *vps4a*^{T248I} mutation results in enlarged endosomal membrane compartments in the**
164 **CNS**
165 Using RNA-FISH, we found that the expression of *vps4a* transcripts is ubiquitous at 5 dpf, with
166 higher levels expressed in the CNS and retina (Fig 2A). In light of the higher expression of
167 *vps4a* in the CNS and the neurological disorder in human patients, we focused our attention on
168 the larval brain. As stated previously, Vps4a mediates the formation of multivesicular bodies
169 from late endosomes. To determine if the mutation affects this function in the nervous system,
170 we performed *in vivo* imaging of LysoTracker, a vital dye that accumulates in acidic membrane
171 compartments such as low pH endosomal compartments. As shown in Fig 2B, endocytic
172 compartments in *vps4a*^{T248I} mutants labeled more brightly with LysoTracker compared to wild-
173 type siblings. The average size and pixel density of acidic membrane compartments in the
174 hindbrain were quantified and we found that *vps4a*^{T248I} mutants have significantly larger acidic
175 membrane compartments (p = 0.0015, n_{WT} = 7, $n_{vps4a(T248I)}$ = 10, t = 3.873, df = 15) (Fig 2C, left
176 panel) that take up more dye (p = 0.0020, n_{WT} = 7, $n_{vps4a(T248I)}$ = 10, t = 3.744, df = 15) (Fig 2C,
177 right panel). Together, these results imply that the *vps4a*^{T248I} mutation has a detrimental effect
178 on endocytic compartment processing in the CNS.
179
180 ***In vivo* imaging reveals a reduction of circulating exosomes in the CNS of *vps4a*^{T248I}**
181 **mutants**
182 Given the known role of Vps4a in multivesicular body formation, we examined whether the
183 mutation affects the number of exosomes that are released upon fusion of multivesicular bodies
184 to the plasma membrane. To detect circulating exosomes in live fish, we used CD63-pHluorin,
185 a pH-sensitive GFP reporter that is quenched in intraluminal vesicles in low pH multivesicular
186 bodies and fluoresces when these vesicles are released into a higher pH extracellular milieu as
187 exosomes [36]. We microinjected a plasmid for ubiquitous expression of CD63-pHluorin into
188 single-cell stage embryos, and selected for larvae that transiently expressed the CD63-pHluorin

189 based on signal in the muscle cells, which is readily detectable by 3 dpf (Fig 3A). The plasma
190 membrane of muscle cells was commonly labeled in our injected fish as was previously reported
191 [36] and served as a positive control for expression. We detected a strong reduction in CD63-
192 phluorin signal in the CNS blood vessels on 3 dpf (Fig 3B), as well as in the midbrain ventricle of
193 4 dpf *vps4a*^{T248I} mutants (Figs 3C,D). We quantified the CD63-pHluorin signal in the midbrain
194 ventricle and normalized to background signal from the surrounding CNS tissue. The
195 relationship between CD63-pHluorin signal in the midbrain ventricle is moderately correlated to
196 signal in the muscle cells in wild-type siblings but not in mutants (Fig 3E). We then calculated a
197 ratio of the normalized pixel intensity of the midbrain ventricle CD63-pHluorin signal to the
198 muscle cell CD63-pHlourin signal and found that the ventricle/muscle cell intensity ratio is
199 significantly decreased in *vps4a*^{T248I} mutants compared to wild-type siblings (p = 0.0382 (exact),
200 n_{WT} = 16, $n_{vps4a(T248I)}$ = 8, Mann-Whitney test) (Fig 3F). This result indicates that there is a
201 decrease in the number of exosomes present in the brain ventricle of mutants, supporting the
202 hypothesis that biogenesis of these extracellular vesicles is reduced by the *vps4a*^{T248I} mutation.
203

204 **Transcriptional changes in the *vps4a*^{T248I} mutant**

205 Considering the broad changes in endosomal morphology and the reduction in circulating
206 exosomes in the CNS of *vps4a*^{T248I} mutants, we next examined the gross morphology of the
207 brain. Using whole mount immunohistochemistry, we labelled the axonal fibers of mutants and
208 siblings with acetylated tubulin antibody to visualize axon morphology. No obvious changes in
209 gross morphology between wild-type siblings and *vps4a*^{T248I} mutants were apparent (Fig 4A).
210 However, we noted the presence of pyknotic nuclei (Fig 4B), which are associated with cell
211 death [37]. We quantified the number of these abnormal cells and found that *vps4a*^{T248I} mutants
212 have significantly more abnormal cells in the CNS compared to wild-type siblings (p < 0.0001
213 (exact), n_{WT} = 9, $n_{vps4a(T248I)}$ = 11, Mann-Whitney Test).

214 As exosomes carry cargo containing microRNA and DNA and have been implicated in
215 the regulation of DNA transcription [38], we assayed for transcriptional changes in the *vps4a*^{T248I}
216 mutant by performing a differential gene expression analysis on a bulk RNAseq data set that
217 was initially used to find the mutation. We then used HCR RNA-FISH to validate the top $\log_2$
218 fold changes in gene expression. We found that the immediate early response genes *atf3* and
219 *jun,* and the axonal regeneration gene *gap43* were dramatically upregulated in mid- and
220 hindbrain regions in the *vps4a*^{T248I} larvae (Fig 4C, D). These striking changes in gene
221 expression are consistent with a failure in intercellular communication by exosomes, and/or
222 endosomal processing within neurons.
223

224 **Impaired vision in *vps4a*^{T248I} mutants**

225 The clinical profile of human patients with missense mutations in *VPS4A* includes visual deficits
226 with a range of symptoms such as retinal dystrophy and cataract formation [5,7]. Although we
227 did not observe expanded melanophores in the *vps4a*^{T248I} mutant, which are indicative of
228 blindness in larvae, we did find pronounced changes in visual function and gene expression in
229 the retina. The optomotor response (OMR) in zebrafish is a reflex that can be evoked by a
230 visual stimulus such as moving stripes, which causes the fish to swim in the direction of
231 perceived motion, resulting in stabilization relative to the environment [39]. Compared to wild-
232 type siblings, *vps4a*^{T248I} mutant larvae have a greatly reduced OMR, suggesting they are blind
233 ($p < 0.0001$ (exact), $n_{WT} = 12$, $n_{vps4a(T248I)} = 10$, Mann-Whitney test) (Fig 5A). To investigate this
234 defect further, we recorded electroretinograms (ERG) to assess the light induced changes in the
235 electrical potential of the whole retina. The b-wave amplitude generated from an ERG can
236 provide insight into the function of the outer retina [40]. A range of light intensities (from the
237 dimmest at log-4, to the brightest at log0) were tested and we found that the b-wave amplitude
238 in *vps4a*^{T248I} mutants is significantly decreased compared to wild-type siblings (log 0, $p <$

239 0.0001, n_{WT} = 23, $n_{vps4a(T248I)}$ = 34; log -1, $p < 0.0001$, n_{WT} = 23, $n_{vps4a(T248I)}$ = 33; log -2, $p <$

240 0.0001, n_{WT} = 23, $n_{vps4a(T248I)}$ = 34; log -3, $p = 0.0101$, n_{WT} = 23, $n_{vps4a(T248I)}$ = 34; log -4, $p =$

241 0.9527, n_{WT} = 23, $n_{vps4a(T248I)}$ = 34, Dunn's multiple comparisons test) (Fig 5B). In addition, we

242 found that *jun* and *gap43* are upregulated in the retina of *vps4a*^{T248I} mutants, specifically in the

243 photoreceptor and retinal ganglion layers (Fig 5C). We also detected reduced *opn1sw1*

244 expression in the photoreceptors of mutants. Together, these analyses indicate that the

245 *vps4a*^{T248I} mutants have pronounced visual defects originating in the retina. Notably, the

246 decrease in b-wave amplitude is variable among individual mutants and may not fully explain

247 the absence of the OMR.

248

249 **Selective vestibular defects in *vps4a*^{T248I} mutants**

250 At the free-swimming stage of development (5 dpf), *vps4a*^{T248I} larvae do not maintain an upright

251 posture, swim sideways or upside down, and do not inflate their swim bladder, which is

252 classically associated with functional deficits in vestibular hair-cells [41]. To further investigate

253 this phenotype in *vps4a*^{T248I} mutant larvae, we tested vestibular function by assessing vestibular

254 induced eye movements (VIEM) [42]. Larvae with loss of hair-cell function mutations have

255 reduced eye movements in response to head rotation [41], however, we did not observe a

256 significant difference between the *vps4a*^{T248I} mutants and wild-type siblings ($p = 0.4632$ (exact),

257 n_{WT} = 18, $n_{vps4a(T248I)}$ = 16, Mann-Whitney test) (Fig 6A). As mutant larvae have pronounced

258 postural defects, we also tested the vestibulospinal reflex (VSR), which assesses vestibular

259 induced motor function in the trunk [43]. We compared the maximum tail angle between wild-

260 type siblings and mutants and found the *vps4a*^{T248I} mutants had a significantly reduced tail angle

261 ($p = 0.0012$ (exact), n_{WT} = 7, $n_{vps4a(T248I)}$ = 10, Mann-Whitney test) (Fig 6B). The normal VIEM

262 along with the reduced VSR result suggests that *vps4a*^{T248I} mutants have selective defects in

263 vestibular pathways.

264 In zebrafish, acceleration of the head is detected by utricular hair cells [42,44,45], which
265 then transmit signals to the utricular afferents of the VIIIth cranial nerve (Fig 6C). The VIIIth
266 nerve innervates the superior vestibular nucleus (SVN), vestibulospinal cell (VS) and tangential
267 nucleus (TAN), as well as the Mauthner cell in the hindbrain [46–49]. Signals from the SVN and
268 TAN are relayed by the oculomotor and trochlear nuclei to oculomotor muscles to produce eye
269 movements associated with the VIEM (Fig 6C;[46,48,50]). VS neurons directly innervate motor
270 neurons in the trunk to produce tail movements [48,50]. To assess the function of the VSR
271 circuit, we used a pan-neuronal GCaMP7a calcium indicator to visualize neuronal activity [51].
272 Recently it was demonstrated that utricular hair cells in zebrafish larvae respond to high
273 frequency tones, analogous to the responses of vestibular hair cells to bone-conducted vibration
274 in mammals [52,53]. To stimulate the vestibular circuitry mediating the VIEM and VSR, we
275 delivered pulses of 600 Hz at 110 dB using a mini-speaker attached to the glass slide on which
276 larvae were mounted for calcium imaging. Electron microscopy data has shown that the lateral
277 dendrite of the Mauthner cell is adjacent to the VS nucleus [48]. To visualize this dendrite, we
278 performed backfill injections of rhodamine dextran prior to calcium imaging, enabling us to use
279 the Mauthner cell as a landmark for the approximate locations of the SVN, VS and TAN (Fig
280 6D). Upon tone stimulation, neurons in all three nuclei responded with an increase in
281 fluorescence (Fig 6D'). Nevertheless, the average raw fluorescence trace for the VS region has
282 a slightly lower peak amplitude in the *vps4a*^{T248I} mutant compared to wild-type siblings (Fig 6E,
283 right). Analysis of the group data from individual fish indicates that the percentage change in
284 normalized fluorescence in the VS region is reduced in *vps4a*^{T248I} mutants (p = 0.0337 (exact),
285 n_{WT} = 11, $n_{vps4a(T248I)}$ = 15, t = 2.252, df = 24)(Fig. 6F, right). As predicted by our behavioral
286 analysis, we did not observe a significant difference in the raw fluorescence trace or percentage
287 change in normalized fluorescence in the TAN or SVN between *vps4a*^{T248I} mutants and wild-
288 type siblings (TAN p = 0.6224 (exact), SVN p = 0.1405 (exact), n_{WT} = 11, $n_{vps4a(T248I)}$ = 15, t =
289 0.4988 (SVN), df = 24 (SVN), t = 1.524 (TAN), df = 24 (TAN)) (Figs 6E,F, left and center).

290 Overall, our calcium imaging data confirm that the VIEM circuit is intact and suggest that
291 reduced activity in the VS neurons, which directly innervate motor neurons, contributes in part to
292 the reduction in tail movements in response to vestibular cues in the *vps4a*^{T248I} mutants.
293

294 **Intact ascending auditory pathway in *vps4a*^{T248I} mutants**

295 In zebrafish, auditory signals excite saccular hair cells, which are innervated by the afferent
296 neurons of the statoacoustic ganglion (or VIIIth nerve). If the auditory cues are sufficiently loud
297 enough to startle, the signal is transmitted to the giant escape fiber neuron known as the
298 Mauthner cell, which directly activates motor neurons[54–56]. Less intense sounds activate
299 hindbrain neurons within the medial octavolateralis nuclei region, which then communicate with
300 the torus semicircularis for further auditory processing [45,57–59] (Fig 7A). *vps4a*^{T248I} mutant
301 larvae are largely unresponsive to tapping on the petri dish, suggesting that hearing is
302 profoundly impaired. We assessed the severity of this defect by quantifying the auditory evoked
303 behavioral response (AEBR), which is a startle response to loud, pure tone stimuli. *vps4a*^{T248I}
304 mutant larvae responded to pure tones significantly less compared to wild-type siblings,
305 indicating that mutants have pronounced defects ($p < 0.0001$ (exact), $n_{WT} = 15$, $n_{vps4a(T248I)} = 20$,
306 Mann-Whitney test) (Fig 7B). The pan-neuronal GCaMP7a calcium indicator was used to
307 examine neuronal activity in the saccular hair cells and statoacoustic ganglion in response to
308 the same 110 dB 600 Hz stimulus (Figs 7C,D). In saccular hair cells, we observed robust
309 responses in average raw fluorescence traces (Fig 7E) and comparable calcium transients in
310 wild-type or mutant individual fish ($p = 0.4162$ (exact), $n_{WT} = 20$, $n_{vps4a(T248I)} = 13$, $t = 0.8228$, df =
311 35) (Fig 7F). Comparable responses were also seen in the statoacoustic ganglion ($p = 0.8748$
312 (exact), $n_{WT} = 20$, $n_{vps4a(T248I)} = 13$, $t = 0.1588$, df = 31) (Figs 7E,F). These results are consistent
313 with LysoTracker labeling, which shows no significant difference in dye uptake between wild-
314 type siblings and *vps4a*^{T248I} mutant in hair cells in the saccule (S1 Figs A-D; $p = 0.0934$ (exact),

315 n_{WT} = 6, $n_{vps4a(T248I)}$ = 9, t = 1.810, df = 13), utricle (p = 0.6314 (exact), n_{WT} = 6, $n_{vps4a(T248I)}$ = 9, t =
316 0.4913, df = 13) or anterior cristae (p = 0.3233 (exact), n_{WT} = 10, $n_{vps4a(T248I)}$ = 10, t = 1.016, df =
317 18). We also examined the saccular hair cells and statoacoustic ganglion for changes in gene
318 misexpression but did not detect transcriptional changes in these tissues (S1 Fig E).

319 The auditory circuitry within the hindbrain for non-startle responses is less well defined
320 in larvae, therefore we focused on a midbrain region of the ascending auditory pathway and
321 examined neuronal activity in the torus semicircularis, which is akin to the inferior colliculus in
322 mammals and key for auditory processing [57,60,61]. This midbrain structure is located
323 beneath the optic tectum at the level of the semicircular canals and saccule of the inner ear and
324 the medial longitudinal fasciculus (MLF) (Fig 7G). We observed a visible increase in GCaMP7a
325 reporter activity in the torus semicircularis of both wild-type siblings and *vps4a*^{T248I} mutants after
326 pure tone stimulation (Fig 7H). No significant differences were detected in the average raw
327 fluorescence traces or percentage change in normalized fluorescence between wild-type
328 siblings and *vps4a*^{T248I} mutants for the torus semicircularis (p = 0.9672 (exact), n_{WT} = 11,
329 $n_{vps4a(T248I)}$ = 13, t = 0.04157, df = 22) (Figs 7I,J). Together, these data indicate that the
330 ascending auditory pathway of *vps4a*^{T248I} mutants including the inner ear and central circuitry is
331 functional.

332

333 **Defective sensorimotor transformation in *vps4a*^{T248I} mutants**

334 Although *vps4a*^{T248I} mutants have a greatly reduced acoustic startle response, our data
335 demonstrate that auditory cues activate the ascending auditory pathway. Notably, mutant larvae
336 are not paralyzed, however, they are largely inactive at the free-swimming stage. Therefore, we
337 assessed whether *vps4a*^{T248I} mutants have a general motor system defect that prevents motor
338 responses to sensory cues.

339 To test whether startle reflexes are globally affected, we measured the ability of
340 *vps4a*^{T248I} mutants to produce a deep C-bend of the trunk in response to contact of a stiff probe
341 with the dorsal region of the head. We observed that both wild-type siblings and *vps4a*^{T248I}
342 mutants displayed robust C-bend motions of their trunks in response to touch (Figs 8B,C; p =
343 0.1079 (exact), n_{WT} = 10, $n_{vps4a(T248I)}$ = 11, t = 1.687, df = 19). This result suggests that touch
344 receptors, along with Mauthner cells and other vital components of motor output such as spinal
345 cord neurons, motor neurons, and muscle cells are functional. In addition, axonal fibers in
346 superficial layers of the skin, the hindbrain, and anterior trunk regions did not show any changes
347 in gross morphology in *vps4a*^{T248I} mutants (Fig 8D). These data point to a deficit within central
348 circuitry in *vps4a*^{T248I} mutants as downstream motor components of the startle reflex are
349 unaffected.
350 As described above, auditory signals from the statoacoustic ganglion are directly
351 transmitted to the Mauthner cell, which innervates trunk motor neurons to generate an escape
352 reflex. However, the 110 dB intensity of our tone stimulus did not result in detectable activation
353 of the Mauthner cell soma, which is consistent with a previous imaging study [62]. Instead, we
354 observed a reliable response in the midbrain nucleus of the medial longitudinal fasciculus
355 (nMLF) (Figs 8A, E-H). The nMLF is a vital component of the descending motor system, serving
356 as a command center for forward locomotion [63–70]. The nMLF contains subpopulations of
357 vGlut1 and vGlut2 positive neurons, which control both fast escape-swimming behaviors as well
358 as slow forward locomotion [68,71]. Neurons in the nMLF were recently shown to respond to
359 hindbrain cranial relay neurons (CRN; Fig 8A), which can be activated by aversive auditory
360 stimulation of Mauthner cells, leading to smooth swimming after an initial C-bend response [63].
361 Although the auditory circuitry to the nMLF activated by non-startle stimuli has not been
362 characterized, the nMLF has been implicated in fine postural control via inputs from the TAN of
363 the ascending vestibuloocular pathway [50]. In *vps4a*^{T248I} mutants, activation of neurons in the
364 TAN is comparable to wild-type responses.

365 Considering that the nMLF is central to motor function in response to sensory cues, we
366 compared GCaMP7a signals in this cluster of neurons between wild-type siblings and *vps4a*^{T248I}
367 mutants in response to the 600 Hz stimulus. These midbrain clusters can be identified based on
368 their prominent axonal tracts that descend near the midline (Fig 8E). We found that the peak
369 amplitudes of calcium transients in the average raw fluorescence trace in the mutant were
370 markedly decreased (Figs 8F-G). In addition, the percentage change in normalized
371 fluorescence in the nMLF was significantly reduced in all individual *vps4a*^{T248I} mutants tested (p
372 < 0.0001 (exact), $n_{WT} = 14$, $n_{vps4a(T248I)} = 11$, $t = 6.937$, df = 23) (Fig 8H).
373 We next investigated the neuronal activity of the spinal cord in response to tone
374 stimulation using the pan neuronal GCaMP7a reporter (Fig 8I). The average raw fluorescence
375 trace of the *vps4a*^{T248I} mutants show lower peaks in response to tone stimulation (Fig 8K). In the
376 examples shown in Figure 8J, a second reporter (GCaMP7a expressed under a muscle cell
377 promoter, [72]) in the trunk muscles shows activation in wild-type larva but none in the mutant.
378 Overall, the percentage change in normalized fluorescence is strongly reduced in *vps4a*^{T248I}
379 mutants ($p < 0.0001$ (exact), $n_{WT} = 11$, $n_{vps4a(T248I)} = 9$, Mann-Whitney test) (Fig 8L). Together,
380 our results indicate that tone stimulation fails to trigger responses in the nMLF descending
381 motor pathway and downstream trunk motor neurons in *vps4a*^{T248I} mutants.
382
383
384 **Discussion**
385 Here we present a T248I mutation in *vps4a*, which causes sensorimotor defects in zebrafish
386 larvae. Spanning biochemical to systems level analyses, our study indicates that a reduction in
387 Vps4a enzymatic activity leads to endosomal defects and reduced exosome biogenesis,
388 resulting in pronounced deficits in vision and sensorimotor transformation of auditory and
389 vestibular cues. We suggest that the mechanisms underlying this type of dysfunction in

390 zebrafish may also contribute to the condition seen in human patients with *de novo* mutations in
391 the human *VPS4A* orthologue.
392
393 **Defective disassembly of membrane scission filaments and decreased exosome**
394 **biogenesis**
395 Vps4a plays a key role in ESCRT-III filament disassembly, and the energy required for
396 this function is produced through the ATP hydrolysis activity of Vps4a [14,27,28,73]. Using an
397 equivalent mutation in yeast, T254I, the threonine to isoleucine substitution in the ATPase
398 domain of yeast *Vps4* results strongly reduced ATPase activity and ESCRT-III filament
399 disassembly. Studies of an ATP hydrolysis deficient mutant, $Vps4^{E233Q}$, reveal that a complete
400 loss of ATP hydrolysis abolishes filament disassembly [74]. In contrast, the yeast protein with
401 the T254I mutation still retains a low level of activity. Nevertheless, our *vps4a* CRISPR
402 experiments suggest that the missense mutation is comparable to a null allele, where we
403 observe a similar auditory/vestibular phenotype in multi-gRNA injected fish without gross
404 developmental defects. These observations suggest that select neural circuits are highly
405 sensitive to perturbation of Vps4a activity.
406 ESCRT-III filament disassembly is a key step in membrane scission, which is vital to
407 cellular mechanisms of multivesicular body formation, exosome biogenesis, cytokinesis and
408 neurite severing [75]. Multivesicular bodies form when late endosomal membrane buds inward,
409 and membrane scission that allows the separation of these buds from the membrane results in
410 intraluminal vesicles (ILVs) [14,38,76,77]. The resulting multivesicular bodies can subsequently
411 either fuse to the plasma membrane to release the ILVs into the extracellular matrix, or fuse with
412 lysosomes to promote degradation of its contents [78,79]. Both fates of ILVs are key for
413 maintaining cell homeostasis and signal transduction [80,81]. An early study of protein sorting
414 mutants yeast proposed a model where in Class E *vps* mutant cells, there is a pre-vacuolar or
415 endosome-like organelle that accumulates a quinacrine vital dye because of defective protein

416 trafficking [82]. It has since been established that expression of a dominant negative Vps4, a
417 class E *vps*, or depletion of other ESCRT components, inhibits the formation of multivesicular
418 bodies and the proper sorting of cargo into intraluminal vesicles [83–86]. Using *in vivo* imaging,
419 we observed an increase in LysoTracker labeling in the central nervous system of *vps4a*^{T248I}
420 mutants. This accumulation of dye and enlargement of acidic membrane compartments
421 suggests a failure of invagination of the membrane of endosomes, resulting in endosomal
422 compartments with larger surface areas, a similar phenotype to what was reported in yeast
423 mutants and in human patient fibroblasts [5].
424 ILVs in multivesicular bodies serve as a source of exosomes and are secreted from
425 nearly all cell types and contain a variety of signaling molecules, such as proteins, lipids, and
426 nucleic acids [87–90]. Exosomes have been implicated in a variety of diseases such as various
427 cancers and neurodegenerative diseases due to the vital role exosomes play in intercellular
428 communication [77,91–95]. A previous study on erythroid cells, which found that transferrin
429 receptor trafficking, a process dependent on proper endosomal sorting and exosome secretion,
430 is disrupted in human patients with *de novo VPS4A* mutations [7]. Using a transiently
431 expressed CD63-pHluorin marker to visualize circulating exosomes in live fish, we found a
432 significant reduction in CD63-pHluorin positive exosomes in the CNS blood vessels and
433 hindbrain ventricle of *vps4a*^{T248I} mutants, suggesting a defect in biogenesis. Disruptions to
434 intercellular signaling through exosomes can manifest as transcriptional changes [79,96,97].
435 Indeed, we found that several genes, either associated with transcription (*atf3* and *jun*) or
436 regeneration (*gap43*), are highly upregulated in the hindbrain, midbrain and retina of *vps4a*^{T248I}
437 mutants. Both *atf3* and *jun* are known to be stress response genes, whereas upregulation of
438 *gap43* may be a compensatory response to disruption of axonal processes. Although exosomes
439 mediate cell-to-cell signaling and are important for cellular homeostasis, it is not clear whether
440 the transcriptional changes in *vps4a*^{T248I} mutants are due to (*i*) reduced exosome signaling, or
441 (*ii*) disruptions in endosomal trafficking, or (*iii*) a combination of both defects. Alternatively, other

442 disruptions to membrane scission in the CNS may be involved as well. The expression of stress
443 response genes in the CNS in zebrafish mutants during larval development is consistent with
444 the microcephaly seen in human patients. While we did not observe changes in gross
445 morphology of the CNS, cell death in the brain was evident yet sparse at the larval stage shown
446 here. We speculate that more pronounced defects in cellular homeostasis would be evident in
447 older animals, however, we limited our analyses to early stages of larval development during
448 which we could discern early onset defects.
449
450 **Sensory and motor deficits**
451 Patients with *VPS4A* mutations are reported to have sensory deficits relating to vision
452 [5]. Poor vision is a common feature that can be associated with retinal dystrophy and
453 cataracts. With respect to visual function in the zebrafish mutant, larvae fail to swim in response
454 to moving visual cues and outer retinal responses to light are significantly reduced, signifying
455 defects in vision that align with transcriptional changes in the retina. Nevertheless, the
456 reduction in outer retinal function was variable among mutants, yet the optomotor response was
457 severely reduced in all *vps4a*^{T248I} larvae tested. These results suggests that the loss of
458 photoreceptor function provides only a partial explanation of the absence of motor reflexes
459 associated with vision and is indicative of an inability to transform visual cues into motor output
460 in a subset of mutants. Notably, human patients are reported to have difficulties in fixing and
461 following a moving object. This issue with visual fixation may be due to poor visual acuity or a
462 combination of poor vision and oculomotor pathway dysfunction.
463 Loss of central control of muscle tone, ataxia and motor delays are common traits found
464 in patients with neurodevelopmental disorders, including *VPS4A* patients [5,7]. The *vps4a*^{T248I}
465 phenotype shares some features with these disorders in that mutant larvae lack control over
466 posture and have sensorimotor defects. Vestibulospinal reflexes, which result in corrective
467 movements of the trunk, are greatly diminished in mutants. However, not all vestibular function

468 in lost; *vps4a*^{T248I} mutants still produce eye movements in response to rotation of the head.
469 Consistent with the behavioral data, neurons of the TAN and SVN, which are part of
470 vestibuloocular pathway [46,48], show comparable activity in the *vps4a*^{T248I} mutant to wild-type
471 neurons. This data indicates that perturbation of Vps4a activity does not result in global defects
472 in vestibular function, or in brain function in general, but rather that specific circuits are more
473 sensitive to mutations in *vps4a*. Normal vestibular induced eye movements and activation of
474 TAN and SVN neurons also indicate that excitation of utricular hair cells and vestibular afferent
475 neurons is unaffected in *vps4a*^{T248I} mutants. In contrast to the vestibuloocular pathway, the
476 vestibulospinal circuit is impaired when *vps4a* is mutated. Hindbrain VS neurons, which directly
477 innervate trunk motor neurons, have decreased neuronal activity in mutants. Recently it was
478 shown that ablation of VS neurons leads to modest defects in posture in zebrafish larvae [98],
479 suggesting that other vestibular circuits contribute to postural control. The reduced activation of
480 the vestibulospinal pathway in *vps4a*^{T248I} mutants may therefore only partially account for the
481 inability to maintain an upright posture.
482 Further evidence for a loss in central control of motor responses emerged from our
483 analysis of the absence of an acoustic startle reflex in *vps4a*^{T248I} mutants. Despite the lack of
484 response to aversive acoustic stimuli, *vps4a*^{T248I} mutants have comparable activation of the
485 ascending auditory pathway as seen in wild-type siblings. Deficits in the descending motor
486 pathways or the spinal cord are also not the cause for the absence of the motor output in
487 response to visual or tone stimulation. *vps4a*^{T248I} mutants are not paralyzed and aversive touch
488 stimuli activate escape responses, demonstrating that mutant larvae can generate robust tail
489 movements. The above experiments indicate that both saccular afferent neurons and Mauthner
490 cells are activated by sensory cues in *vps4a*^{T248I} mutants, implying that a second pathway may
491 be defective in generating acoustic startle reflexes. One such pathway may involve hindbrain
492 spiral fiber neurons, which have been shown to be essential for Mauthner cell-dependent
493 escape responses [99]. Nevertheless, our *in vivo* imaging experiments using a non-startle tone

494 stimulus revealed a pronounced reduction in the activity of midbrain nMLF neurons and
495 downstream spinal cord neurons of *vps4a*^{T248I} mutants. Neurons of the nMLF play a key role in
496 receiving sensory input and sending motor commands to the spinal cord and are thought to play
497 an analogous role to the interstitial nucleus of Cajal in the mammalian midbrain, which controls
498 eye and head movements [66,68,100]. In zebrafish, both visual and vestibular systems provide
499 sensory input to the nMLF [46,101,102]. Interestingly, TAN neurons of the vestibuloocular
500 pathway, also play a dual role of controlling eye and body movements in zebrafish. TAN
501 neurons, which project to the nMLF [46], were recently shown to transmit signals about the roll
502 axis of the body to the nMLF, implicating this circuit in fine control of posture [50]. In *vps4a*^{T248I}
503 mutants, TAN neurons are also activated by the tone stimulus, yet postural defects are
504 pronounced, further bolstering the notion that sensory input such as vestibular cues fail to
505 trigger sensorimotor transformation within the nMLF.
506
507 In summary, our combined biochemical and *in vivo* analyses have revealed that loss of
508 Vps4a function generates sensorimotor processing defects in the CNS of zebrafish larvae. Our
509 study provides a better understanding of the cause of motor dysfunction when *vps4a* is mutated
510 and has implications for potential therapies as well. In emerging work on exosomes as
511 therapeutical reagents, these extracellular vesicles, which can cross the blood brain barrier, can
512 serve as both a diagnostic tool and as a potential vehicle for delivery [103]. Recent studies
513 have shown that exosome therapy can aid in sensorimotor recovery after injury or resulting from
514 acute or chronic neurodegenerative diseases [104–106], thus there is potential for exosomes to
515 be used in early neurodevelopmental disorders such as those associated with *VPS4A*.
516
517
518
519

Materials and Methods

Zebrafish care and use

We maintained zebrafish lines for the *vps4a*^{T248I} allele in the Top Long Fin (TLF) wild-type (WT) or *mitfa*^{b692} *nacre* backgrounds. The *vps4a*^{T248I} Tg(α-tubulin-gal4;MP-gal4;cmlc2-GFP;UAS-GCaMP7a) line was generated by crossing into a *mitfa*^{b692} Tg(α-tubulin-gal4;MP-gal4;cmlc2-GFP;UAS-GCaMP7a) fish line (a gift from Philippe Mourrain). The MP-gal4 transgene was present in most fish, marking the muscle cells as well. Breeding stocks were housed at 28.5°C and animal husbandry followed standard zebrafish methods for laboratory utilization [107], as approved and overseen by the Institutional Animal Care and Use Committees at both Oregon Health and Sciences University and Stanford University. The experiments used zebrafish larvae 3-7 days post fertilization (dpf) before gender differentiation occurs. Embryos and larvae were raised in E3 medium (0.33 mM CaCl2, 0.17 mM KCl, 0.33 mM MgSO4, and 5 mM NaCl) incubated at 28.5°C. When appropriate, larvae were anesthetized in E3 with 0.03% 3-amino benzoic acid ethylester (MESAB, Western Chemical) to minimize pain and distress.

Genotyping Methods

For the *vps4a*^{T248I} allele, we genotyped fish and larvae using kompetitive allele-specific PCR (KASP) genotyping (LGC Biosearch Technologies) per the manufacturer's instructions.

Identification of raumschiff mutant allele

Positional cloning was performed using simple sequence length polymorphism (SSLP) markers mapped to the zebrafish genome [108]. 5 dpf zebrafish larvae were sorted by phenotype.

For Whole Genome Sequencing, 5 dpf zebrafish larvae were sorted into separate pools of 20 homozygous mutants and 20 heterozygous and homozygous wild-type siblings. Genomic DNA was collected using a DNeasy Blood & Tissue Kit (Qiagen) and samples were processed by Azenta Life Sciences (formerly GENEWIZ) for library preparation and Illumina HiSeq

546 sequencing. The resulting .gz files were uploaded to SNPTrack
547 (http://genetics.bwh.harvard.edu/snptrack/) to identify the mutation.
548
549 **CRISPR injections**
550 Single guide RNAs against *vps4a* and *vps4b* were designed using the CHOPCHOP website
551 (https://chopchop.cbu.uib.no/) and synthesized (Alt-R CRISPR-Cas9 System, IDT). Three
552 guides were chosen based on if they targeted the ATPase domain or additional exons common
553 to all isoforms, low number of off target sites and efficiency. Multi-guide CRISPR injections
554 were performed as described previously [30]. Briefly, crRNA and tracrRNA guides were
555 combined in equal molar amounts in Duplex Buffer (IDT), and this RNA Duplex mix was
556 combined with 1 µg/µL Cas9-NLS protein (PNA Bio). 1 nL of RNA guide-CAS9 mixture was
557 injected into single cell stage TLF wildtype embryos. Embryos were checked daily for viability
558 and auditory/vestibular phenotypes scored on 5 dpf.
559
560 **Protein expression and purification**
561 *Saccharomyces cerevisiae* Vps4 (wild-type), and mutant Vps4(T254I) were cloned into the
562 pET28a vector with an N-terminal His6 tag. The two proteins were expressed in Escherichia coli
563 BL21 (DE3) strains and induced with 1 mM IPTG at 20°C overnight. Sonication was used to lyse
564 cells and centrifuged the lysates. The supernatant was loaded into Ni–NTA beads (GE
565 Healthcare) and the eluates were incubated with 5 U mL−1 apyrase (Sigma-Aldrich) at 4°C
566 overnight. All proteins were further purified by SEC using a Superdex 200 10/300 GL column
567 (GE Healthcare) with 20 mM Tis-HCl at pH 8.0, 150 mM NaCl buffer. The purity and quality of all
568 the proteins were tested by SDS–PAGE and Nano-drop (Implen).
569 *Saccharomyces cerevisiae* Snf7 mutant (R52E) and Vps24 were cloned into the pET28a
570 vector with an N-terminal His6 tag. The two proteins were expressed in Escherichia coli BL21
571 (DE3) strains and induced with 1 mM IPTG at 20°C overnight. Sonication was used to lyse cells

572 and centrifuged the lysates. The supernatant was loaded to a Ni–NTA beads (GE Healthcare)
573 and the elute was further purified by SEC using a Superdex 200 10/300 GL column (GE
574 Healthcare) with 20 mM Tis-HCl at pH 8.0, 150 mM NaCl buffer. The purity and quality of all the
575 proteins were tested by SDS–PAGE and Nano-drop (Implen).
576 *Saccharomyces cerevisiae* Vps2 were cloned into the pET28a vector with an N-terminal
577 MBP-His6 -TEV-tag. We expressed the resulting Vps2 construct in E.coli BL21 (DE3) at 20°C
578 for 16 hours with 1 mM IPTG. We purified the protein using Ni–NTA resin (GE Healthcare). We
579 mixed the eluted fractions from the His column with TEV (tobacco etch virus) protease for 3
580 hours at 4°C. We then loaded the cleaved samples onto a 5 mL HiTrap Q-sepharose FF column
581 (GE Healthcare) and eluted the material with a gradient of 0%-100% buffer (20 mM Tris-HCl, pH
582 8.0, 500 mM NaCl) in 50 column volumes.
583
584 **Sedimentation Analysis of Filament Disassembly**
585 Yeast ESCRT III filaments were assembled by mixing Snd7(R52E), Vps24 and Vps2 in a
586 molar ratio of 2:1:1 at room temperature for 1 hour. Then, the formed filaments were centrifuged
587 at 50,000 r.p.m. for 30 minutes in a TLA-100 ultracentrifuge rotor (Beckman Coulter). The pellet
588 was resuspended in the buffer containing 20 mM Tris-HCl at pH 8.0, 150 mM NaCl. The pellet
589 (P) and supernatant (S) were analyzed by SDS–PAGE.
590 For sedimentation analysis of ESCRT III filament disassembly, filaments were mixed
591 with 5 μM Vps4 or Vps4(T254I) in 20 mM Tris-HCl at pH 8.0, 150 mM NaCl, 2 mM MgCl2 buffer,
592 separately. Reactions were started by adding ATP to a final concentration of 5 mM. After
593 incubation at room temperature for 10 minutes, reactions were stopped by adding EDTA to a
594 final concentration of 50 mM. Samples were then subjected to ultracentrifugation and analyzed
595 via SDS-PAGE and negative staining.
596
597 **ATPase activity assay**

598 ATPase activities were determined for wild-type and mutant Vps4 proteins using the
599 Quantichrome ATPase/GTPase Assay Kit (BioAssay Systems) at room temperature. Briefly,
600 5 μM Vps4 or mutant Vps4(T254I) protein was added to ATPase assay buffer and 4 mM ATP for
601 30 minutes, and then stopped using reagent from the kit. The solution was incubated at room
602 temperature for 30 minutes, and immediately the absorbance at 620 nm was detected using a
603 plate reader (Enspire, Perkin Elmer). The released phosphate was calculated based on the
604 absorbance standard curve established using KH_2PO_4 standards.
605
606 **Auditory-evoked behavioral response (AEBR)**
607 AEBR was tested as described previously [109,110] using the Zebrabox system (ViewPoint Life
608 Sciences). 5 dpf wild-type siblings or *vps4a*^{T248I} mutant larvae were confined to wells of a 96-
609 well plate in 200 μL E3 per well, in the dark. Larvae were subjected to 100 millisecond, 1kHz
610 pure tones at 157 decibel sound pressure (dB SPL, relative to 1mPA) every 2 seconds for 1
611 minute. An infrared camera recorded larval movements and ZebraLab tracking software
612 documented pixel changes, which represent movement over time for each larva. To distinguish
613 between evoked responses and spontaneous background movement, movements within 1
614 second before a stimulus were excluded from a given trial. For each larva, the positive
615 responses were calculated as a percentage out of total possible response within a minute, and
616 the best of three trials was used for analysis.
617
618 **Vestibulospinal Reflex (VSR)**
619 The device and method used to test the VSR was done as previously described [43,44]. Briefly,
620 5 dpf larvae were embedded dorsal-up in 2% prewarmed low melt agarose in E3 media without
621 anesthetic on a mounting chamber. The agarose around the trunk and pectoral fins was
622 carefully removed and replaced with 20 μL E3 media, and the mounting chamber was placed in

623 the device. A motor rocks the platform from −75° to + 75° at 0.53 Hz, and an infrared camera
624 recorded video of the reflex at 30 fps (1280 frames).
625 Modified ZebraZoom software [111] tracks the movements of the trunk at regular
626 intervals and calculates the real tail angle over time between the X axis and the axis formed by
627 the tip of the tail and the center of the swimming bladder.
628
629 **Vestibular-induced eye movement (VIEM)**
630 The VIEM experiment was done similarly as described previously using a modified device
631 [42,44]. 5 dpf larvae were embedded on a small cover slip in prewarmed 2% low melt agarose
632 in E3 buffer, without anesthetic. Agarose surrounding the eyes was gently removed and
633 replaced with approximately 10 μL of E3 media to permit free eye moment. The mounted larvae
634 were positioned vertically, head down, between an infrared camera and an infrared LED array
635 on a programmable rocking platform. Larvae kept in darkness during the experiment. The
636 platform rocked (-45° to 45°) at 0.25 Hz frequency for 60 seconds while larval eye movements
637 were video recorded in infrared.
638 Software-based video analyses quantified the amplitudes of angular eye movements as
639 a function of their frequency of repetition. Larvae with normal VIEM show peak movement
640 amplitude at 0.25 Hz, in synchrony with platform rotation. Baseline spontaneous eye movement,
641 taken as the average amplitude across all quantified frequencies, was subtracted to determine
642 the VIEM amplitude at 0.25 Hz. We calculated the normalized amplitude of the eye ratio for
643 each larva and used the two-tailed unpaired t test with Welch's correction to compare mutants
644 to their corresponding siblings.
645
646 **Touch Startle Reflex**

647 Touch Startle was performed by mounting 7 dpf zebrafish larvae similarly to the VSR mounting
648 method. A micromanipulator holding a borosilicate glass capillary tube (Sutter, #BF150-86-10)
649 pulled into a needle was used to touch the head of the larvae. Startle movements were
650 recorded by a Hamamatsu C11440 ORCA-Flash 2.8 camera at 100 fps. Quantification of C-
651 bends was performed as described in [112].
652
653 **Optomotor Reflex (OMR)**
654 To test for the optomotor reflex, we adapted the assay from Neuhauss et al., 1999. A set of 4
655 tracks (each lane measuring at 12 cm x 0.6 cm) and comb that fit between the lanes, was
656 constructed using 3D printing. The lanes were placed in a 15 cm petri dish (VWR) and filled
657 partially with E3 buffer. The comb was inserted to block the starting end of the lanes, and 5-6
658 dpf larvae were placed in the starting area of the lanes. The petri dish was placed over a
659 screen that plays a video of 0.5 cm stripes. To record the movement of the larva along the
660 lanes, a camera was mounted above the petri dish. To perform the experiment, the video of
661 stripes was played, and the comb was removed, allowing larva to swim against the movement
662 of stripes to the end of the lane. To quantify this reflex, screenshots of the video were taken of
663 the larva in the starting region of the lane prior to comb removal and then 30 seconds after the
664 comb was removed. The distance between the location of each larva prior to comb removal
665 and 30 seconds after was measured in ImageJ in millimeters.
666
667 **Electroretinogram (ERG)**
668 ERG recordings were performed on 5 - 6 dpf mutant and wild-type sibling larvae, as described
669 in [40,113]. b-wave amplitudes were plotted and analyzed using Dunn's multiple comparisons.
670
671 **Immunohistochemistry**

672 Larvae were fixed with 4% PFA, dehydrated with Methanol, rehydrated using a graded series of
673 PBSDT (1x PBS with 0.25% Tween-20 and 1% DMSO): Methanol and then treated with 150
674 mM Tris-HCl for antigen retrieval. Samples were then washed and permeabilized with ice cold
675 100% acetone, followed by more washes. Samples were blocked for 2 hours at room
676 temperature with 6% goat serum and 3% BSA, then incubated overnight with 1:1000 anti-
677 acetylated tubulin rabbit primary antibodies (ThermoFisher). Samples were then incubated
678 overnight with 1:1000 anti-rabbit Alexa 488 (Invitrogen) secondary antibodies, protected from
679 light.
680
681 **Lysotracker**
682 5 dpf PTU-treated larva were sorted and placed in mutant-sibling pairs in a 2 mL Eppendorf
683 tube. LysoTracker Red DND-99 (Invitrogen) was diluted to 1:100 to examine brains or 1:200 to
684 examine inner ear hair cells. The larvae were incubated in Lysotracker for 40 minutes at 28.5°C
685 with the tube left open but protected from light. The larvae were then washed with E3 buffer for
686 10 minutes and immediately imaged.
687 Hindbrain lysotracker uptake was quantified by selecting a single Z-stack slice of the
688 hindbrain region and thresholding it to highlight particles in the size range of endosomal
689 compartments (size = 0.02-2 μm). The integrated density and area of particles from two equally
690 sized regions of interest from hindbrain sections and a single region of neuropil were measured
691 from each slice using the Analyze Particles function of Fiji. The integrated density
692 measurements were averaged and normalized to the integrated density of the neuropil.
693
694 **CD63-phluorin Injections and Analysis**
695 pUbi-CD63-pHluorin was a gift from Frederik Verweij and was generated as described in [114].
696 Nacre-background *vps4a*^{T248I} mutant and sibling embryos were injected at the one cell stage
697 with 100 ng/μL pUbi-CD63-pHluorin. Damaged embryos were sorted out, and only larvae with

698 CD63-pHluorin expression on muscle cell membranes were selected for live imaging on 3-4 dpf.
699 Time lapse videos were recorded at 50 fps for 2 minutes at 63x with a 2x optical zoom. For
700 analysis, three frames were combined, and the mean pixel intensity was measured from regions
701 of the ventricular intracranial space, surrounding tissue as background, and muscle cells. The
702 mean pixel intensity of ventricular intracranial space was normalized to background and then
703 divided by muscle cell pixel intensity.
704
705 **Bulk Tissue RNASeq**
706 Total RNA was isolated from 5 dpf wild type and vps4a mutant larvae (n = 15-20 each
707 genotype) using TRIzol reagent (Thermo Fisher, 15596026) according to the manufacturer's
708 protocol. RNA-seq library construction and single-end sequencing were performed by the OHSU
709 Massively Parallel Sequencing Shared Resource (RRID SCR_009984, Oregon Health &
710 Science University, Portland, OR, USA). Sequencing reads were mapped to the Danio rerio
711 GRCz10 genome using Tophat v2.1.1 [115] from within an OSHU instance of the Galaxy
712 sequence analysis platform [116]. The resulting BAM files were imported to SeqMonk v1.42.0
713 (www.bioinformatics.babraham.ac.uk/projects/seqmonk/) for data visualization and statistical
714 analysis using the Intensity Difference filter for unreplicated data sets. Genes with an adjusted
715 p-value < 0.05 were considered differentially expressed.
716
717 **Hybridization Chain Reaction (HCR)**
718 For HCR, custom probes for *vps4a*, *atf3*, *jun*, *gap43, opn1sw1* and the corresponding
719 fluorescent B-amplifier hairpins were ordered from Molecular Instruments
720 (https://www.molecularinstruments.com/). Probes were chosen based on their log2(fold
721 change) and number of reads from bulk RNA sequencing analysis. Probes were assigned B-
722 amplifiers with the intention of doing multi-plex experiments. Probe sequences are considered

723 confidential and proprietary information of Molecular Instruments based on their Terms and
724 Conditions, so further inquiries may be directed to their technical team.
725 PTU-treated larvae were sorted at 5 dpf and fixed overnight in 4% paraformaldehyde
726 (PFA) at 4°C with rocking. After fixation, larvae were washed in PBST (1X PBS with 0.1%
727 Tween-20), dehydrated with a methanol:PBS series (25%, 50% and 75% methanol in PBS),
728 then stored at least overnight at -20°C. Larvae were subsequently rehydrated with a reverse
729 methanol:PBST series, washed several times with PBST, permeabilized for 15 minutes with 20
730 µg/mL Proteinase K, post-fixed with 4% PFA and then washed again. Probe detection and
731 amplification with fluorescent hairpins was performed as recommended by the MI protocol for
732 whole mount zebrafish larva with extended pre-hybridization and pre-amplification times (4
733 hours each) and probe concentrations adjusted based on the reads of each probe (5 nM for
734 *gap43*, 10 nM for *vps4a*).
735
736 **Calcium Imaging**
737 Larvae at 3 dpf *vps4a*^{T248I} *Tg(α-tubulin-gal4:UAS-GCaMP7a)* were sorted for strong GCaMP
738 expression in the brain. 5 dpf GCaMP positive larvae were mounted in 2% low melt agarose on
739 a custom depression slide fitted with a mini-speaker (DAEX-9-45M Skinny Mini Exciter 9 mm 1
740 W 4 Ohm). Using an AIYIMA A07 amplifier, tone stimuli were played through the mini speaker
741 using a custom script in MATLAB (R2020b, MathWorks). 600 Hz (0.35 V) or 450 Hz (0.2 V)
742 tones were played for 0.6 seconds or 0.1 seconds, respectively, five times with 10 second
743 intervals. Time lapse images and fluorescence values were recorded using LAS-X software
744 (Ver 3.7.2.22383). To account for variability in GCaMP7a expression between larvae, all
745 fluorescence values were normalized by subtracting background measurements. Traces were
746 generated by averaging the normalized fluorescence value (F) for each time point across all
747 larvae and plotting this value over time. To calculate percentage change in fluorescence

748 (ΔFt/F0%), 2-3 frames, containing image artifacts (due to the tone stimulation shaking the slide)
749 were identified for each stimulus, and fluorescence values corresponding to these frames were
750 discarded. The F0 measurement was selected from the frame prior to tone stimulation, based
751 on the time lapse video and presence of artifact frames, and Ft was selected as the highest
752 frame immediately after tone stimulation. (ΔFt/F0)/F0 was used to calculate the change in
753 GCaMP7a fluorescence and was multiplied by 100 to convert into a percentage to generate
754 "(ΔFt/F0%)". The average percentage change in fluorescence was then calculated for each
755 larva and differences between wild-type siblings and *vps4a* mutants was analyzed using
756 unpaired t tests.
757
758 **Retrograde Labeling of Mauthner Cells**
759 Retrograde labeling was adapted from previously published methods [117,118]. Larvae were
760 anesthetized with 0.3% MESAB prior to spinal injection of 10mg/mL 10,000 MW
761 Tetramethylrhodamine dextran (10,000 MW, D1866, Thermo Fisher) in PBS. Custom glass
762 injection needles were prepared from borosilicate glass capillaries (TW100F-4, World Precision
763 Instruments) using a micro-needle puller (Suttner Instruments Co, Model P-87) using heat cycle
764 517, pulling cycle 75, velocity 75 and time 90, and then the tip was broken using forceps.
765 Larvae were mounted laterally in 2% low melt agarose for injection, and then incubated in E3
766 media overnight to recover before imaging.
767
768 **Microscopy and Image Processing**
769 Images for LysoTracker, CD63pHluorin, and HCR were take using an upright LSM700 laser-
770 scanning confocal microscope with Zeiss Zen software (Carl Zeiss). For live imaging of larva,
771 they were anesthetized in 0.03% MESAB in E3 media and mounted in 2% prewarmed low melt
772 agarose. Images were collected using 488 nm, 555 nm and 647 nm lasers, depending on the
773 requirements of the individual experiment (Acetylated Tubulin and CD63pHluorin used 488 nm,

774 LysoTracker used 555 nm, HCR used up to all 3 depending on the fluorescent hairpins used).
775 We used a Leica HC PL Fluotar 10x/0.3 lens for Acetylated Tubulin, HCR and LysoTracker
776 images, a Plan Apochromat 40x/1.0DIC lens for LysoTracker quantification images and an
777 Acroplan 63x/0.95W water immersion lens for higher magnification HCR images. Laser power
778 and gain were determined independently for each fluorophore and kept consistent within each
779 experiment. The FIJI build of ImageJ Version 2.1.0/1.53t was used to process all raw image
780 files. For Calcium Signaling, scans were taken using a Leica SP-8 Confocal Microscope
781 equipped with a 20x (NA 1.0) objective, using LAS-X software. Images were collected using
782 488 nm white laser light.
783
784 **Experimental Design and Statistical Analysis**
785 The number of zebrafish larvae used is denoted in the figure legends. G*Power software was
786 used to ensure there were sufficient samples tested. All statistical analyses were performed
787 using GraphPad Prism software (version 9). The data was tested for normal distribution using
788 Shapiro-Wilk test. Data is presented as mean ± SD, and significance between mutant and wild-
789 type sibling groups was determined using unpaired t test unless otherwise noted. The image in
790 figure 1C was adapted from Sun et al., 2017 using Mol* [119] and RCSB PDB (PDB ID:5XMI)
791 software.
792
793 **Acknowledgements:** The authors would like to thank the past members of the Genetics
794 Department of the Max Planck Institute in Tuebingen, Germany, particularly Tatjana Piotrowski
795 and Stefan Schulte-Merker for their assistance in a small-scale allele screen. We would also like
796 to thank Peng Sun for his technical assistance, and Matthew Esqueda and Sivan Brodo-Abo for
797 their help with animal care. This work was supported in part by a National Institute on Deafness
798 and Other Communication Disorders award (DC0170046) and SICHL funding from the OHNS

department of Stanford University to T.N.; a grant from the National Natural Science Foundation of China to S.S. (92254306); Swiss National Science Foundation (310030_204648) to S.N.

References

1. Lewis EM, Kroll KL. Development and disease in a dish: the epigenetics of neurodevelopmental disorders. Epigenomics. 2018;10: 219–231. doi:10.2217/epi-2017-0113

2. Cardoso AR, Lopes-Marques M, Silva RM, Serrano C, Amorim A, Prata MJ, et al. Essential genetic findings in neurodevelopmental disorders. Hum Genomics. 2019;13: 31. doi:10.1186/s40246-019-0216-4

3. Parenti I, Rabaneda LG, Schoen H, Novarino G. Neurodevelopmental Disorders: From Genetics to Functional Pathways. Trends Neurosci. 2020;43: 608–621. doi:10.1016/j.tins.2020.05.004

4. Dan B. Developmental central hypotonia: implications for counselling, prognosis, and management. Dev Med Child Neurol. 2022;64: 4. doi:10.1111/dmcn.15085

5. Rodger C, Flex E, Allison RJ, Sanchis-Juan A, Hasenahuer MA, Cecchetti S, et al. De Novo VPS4A Mutations Cause Multisystem Disease with Abnormal Neurodevelopment. Am J Hum Genet. 2020;107: 1129–1148. doi:10.1016/j.ajhg.2020.10.012

6. Ganguly J, Kulshreshtha D, Almotiri M, Jog M. Muscle Tone Physiology and Abnormalities. Toxins. 2021;13: 282. doi:10.3390/toxins13040282

819 7. Seu KG, Trump LR, Emberesh S, Lorsbach RB, Johnson C, Meznarich J, et al. VPS4A
820 Mutations in Humans Cause Syndromic Congenital Dyserythropoietic Anemia due to
821 Cytokinesis and Trafficking Defects. Am J Hum Genet. 2020;107: 1149–1156.
822 doi:10.1016/j.ajhg.2020.10.013

823 8. Lunati A, Petit A, Lapillonne H, Gameiro C, Saillour V, Garel C, et al. VPS4A mutation in
824 syndromic congenital hemolytic anemia without obvious signs of dyserythropoiesis. Am J
825 Hematol. 2021;96: E121–E123. doi:10.1002/ajh.26099

826 9. Scheuring S, Röhricht RA, Schöning-Burkhardt B, Beyer A, Müller S, Abts HF, et al.
827 Mammalian cells express two VPS4 proteins both of which are involved in intracellular
828 protein trafficking. J Mol Biol. 2001;312: 469–480. doi:10.1006/jmbi.2001.4917

829 10. Strausberg RL, Feingold EA, Grouse LH, Derge JG, Klausner RD, Collins FS, et al. Generation
830 and initial analysis of more than 15,000 full-length human and mouse cDNA sequences.
831 Proc Natl Acad Sci U S A. 2002;99: 16899–16903. doi:10.1073/pnas.242603899

832 11. Babst M, Sato TK, Banta LM, Emr SD. Endosomal transport function in yeast requires a novel
833 AAA-type ATPase, Vps4p. EMBO J. 1997;16: 1820–1831. doi:10.1093/emboj/16.8.1820

834 12. Beyer A, Scheuring S, Müller S, Mincheva A, Lichter P, Köhrer K. Comparative sequence and
835 expression analyses of four mammalian VPS4 genes. Gene. 2003;305: 47–59.
836 doi:10.1016/S0378-1119(02)01205-2

837 13. Monroe N, Han H, Gonciarz MD, Eckert DM, Karren MA, Whitby FG, et al. The oligomeric
838 state of the active Vps4 AAA ATPase. J Mol Biol. 2014;426: 510–525.
839 doi:10.1016/j.jmb.2013.09.043

840 14. Alonso Y Adell M, Migliano SM, Teis D. ESCRT-III and Vps4: a dynamic multipurpose tool for
841 membrane budding and scission. FEBS J. 2016;283: 3288–3302. doi:10.1111/febs.13688

842 15. Babst M, Katzmann DJ, Estepa-Sabal EJ, Meerloo T, Emr SD. Escrt-III: an endosome-
843 associated heterooligomeric protein complex required for mvb sorting. Dev Cell. 2002;3:
844 271–282. doi:10.1016/s1534-5807(02)00220-4

845 16. Ott C, Nachmias D, Adar S, Jarnik M, Sherman S, Birnbaum RY, et al. VPS4 is a dynamic
846 component of the centrosome that regulates centrosome localization of γ-tubulin,
847 centriolar satellite stability and ciliogenesis. Sci Rep. 2018;8: 3353. doi:10.1038/s41598-
848 018-21491-x

849 17. Cacheiro P, Muñoz-Fuentes V, Murray SA, Dickinson ME, Bucan M, Nutter LMJ, et al. Human
850 and mouse essentiality screens as a resource for disease gene discovery. Nat Commun.
851 2020;11: 655. doi:10.1038/s41467-020-14284-2

852 18. Loncle N, Agromayor M, Martin-Serrano J, Williams DW. An ESCRT module is required for
853 neuron pruning. Sci Rep. 2015;5: 8461. doi:10.1038/srep08461

854 19. Haffter P, Granato M, Brand M, Mullins MC, Hammerschmidt M, Kane DA, et al. The
855 identification of genes with unique and essential functions in the development of the
856 zebrafish, Danio rerio. Development. 1996;123: 1–36. doi:10.1242/dev.123.1.1

857 20. Vaz R, Hofmeister W, Lindstrand A. Zebrafish Models of Neurodevelopmental Disorders:
858 Limitations and Benefits of Current Tools and Techniques. Int J Mol Sci. 2019;20: 1296.
859 doi:10.3390/ijms20061296

860 21. de Abreu MS, Genario R, Giacomini ACVV, Demin KA, Lakstygal AM, Amstislavskaya TG, et
861 al. Zebrafish as a Model of Neurodevelopmental Disorders. Neuroscience. 2020;445: 3–11.
862 doi:10.1016/j.neuroscience.2019.08.034

863 22. Fetcho JR. The utility of zebrafish for studies of the comparative biology of motor systems. J
864 Exp Zoolog B Mol Dev Evol. 2007;308B: 550–562. doi:10.1002/jez.b.21127

865 23. Bandmann O, Burton EA. Genetic zebrafish models of neurodegenerative diseases.
866 Neurobiol Dis. 2010;40: 58–65. doi:10.1016/j.nbd.2010.05.017

867 24. Kalueff AV, Stewart AM, Gerlai R. Zebrafish as an emerging model for studying complex
868 brain disorders. Trends Pharmacol Sci. 2014;35: 63–75. doi:10.1016/j.tips.2013.12.002

869 25. Sakai C, Ijaz S, Hoffman EJ. Zebrafish Models of Neurodevelopmental Disorders: Past,
870 Present, and Future. Front Mol Neurosci. 2018;11. Available:
871 https://www.frontiersin.org/articles/10.3389/fnmol.2018.00294

872 26. Leshchiner I, Alexa K, Kelsey P, Adzhubei I, Austin-Tse CA, Cooney JD, et al. Mutation
873 mapping and identification by whole-genome sequencing. Genome Res. 2012;22: 1541–
874 1548. doi:10.1101/gr.135541.111

875 27. Davies BA, Azmi IF, Payne J, Shestakova A, Horazdovsky BF, Babst M, et al. Coordination of
876 substrate binding and ATP hydrolysis in Vps4-mediated ESCRT-III disassembly. Mol Biol
877 Cell. 2010;21: 3396–3408. doi:10.1091/mbc.E10-06-0512

878 28. McCullough J, Frost A, Sundquist WI. Structures, Functions, and Dynamics of ESCRT-III/Vps4
879 Membrane Remodeling and Fission Complexes. Annu Rev Cell Dev Biol. 2018;34: 85–109.
880 doi:10.1146/annurev-cellbio-100616-060600

881 29. Wu RS, Lam II, Clay H, Duong DN, Deo RC, Coughlin SR. A Rapid Method for Directed Gene
882 Knockout for Screening in G0 Zebrafish. Dev Cell. 2018;46: 112-125.e4.
883 doi:10.1016/j.devcel.2018.06.003

884 30. Kroll F, Powell GT, Ghosh M, Gestri G, Antinucci P, Hearn TJ, et al. A simple and effective F0
885 knockout method for rapid screening of behaviour and other complex phenotypes. Ekker
886 SC, Stainier DY, Balciunas D, editors. eLife. 2021;10: e59683. doi:10.7554/eLife.59683

887 31. Yang Q, Chen D, Xiong F, Chen D, Liu C, Liu Y, et al. A splicing mutation in VPS4B causes
888 dentin dysplasia I. J Med Genet. 2016;53: 624–633. doi:10.1136/jmedgenet-2015-103619

889 32. Hanovice NJ, Daly CMS, Gross JM. N-Ethylmaleimide–Sensitive Factor b (nsfb) Is Required
890 for Normal Pigmentation of the Zebrafish Retinal Pigment Epithelium. Invest Ophthalmol
891 Vis Sci. 2015;56: 7535–7544. doi:10.1167/iovs.15-17704

892 33. Woods IG, Lyons DA, Voas MG, Pogoda H-M, Talbot WS. nsf Is Essential for Organization of
893 Myelinated Axons in Zebrafish. Curr Biol. 2006;16: 636–648.
894 doi:10.1016/j.cub.2006.02.067

895 34. Gao Y, Khan YA, Mo W, White KI, Perkins M, Pfuetzner RA, et al. Sensory deficit screen
896 identifies nsf mutation that differentially affects SNARE recycling and quality control. Cell
897 Rep. 2023;42: 112345. doi:10.1016/j.celrep.2023.112345

898 35. Sun S, Li L, Yang F, Wang X, Fan F, Yang M, et al. Cryo-EM structures of the ATP-bound
899 Vps4E233Q hexamer and its complex with Vta1 at near-atomic resolution. Nat Commun.
900 2017;8: 16064. doi:10.1038/ncomms16064

901 36. Verweij FJ, Bebelman MP, Jimenez CR, Garcia-Vallejo JJ, Janssen H, Neefjes J, et al.
902 Quantifying exosome secretion from single cells reveals a modulatory role for GPCR
903 signaling. J Cell Biol. 2018;217: 1129–1142. doi:10.1083/jcb.201703206

904 37. Hou L, Liu K, Li Y, Ma S, Ji X, Liu L. Necrotic pyknosis is a morphologically and biochemically
905 distinct event from apoptotic pyknosis. J Cell Sci. 2016;129: 3084–3090.
906 doi:10.1242/jcs.184374

907 38. Kalluri R, LeBleu VS. The biology, function, and biomedical applications of exosomes.
908 Science. 2020;367: eaau6977. doi:10.1126/science.aau6977

909 39. Kist AM, Portugues R. Optomotor Swimming in Larval Zebrafish Is Driven by Global Whole-
910 Field Visual Motion and Local Light-Dark Transitions. Cell Rep. 2019;29: 659-670.e3.
911 doi:10.1016/j.celrep.2019.09.024

912 40. Niklaus S, Cadetti L, Berg-Maurer CM vom, Lehnherr A, Hotz AL, Forster IC, et al. Shaping of
913 Signal Transmission at the Photoreceptor Synapse by EAAT2 Glutamate Transporters.
914 eNeuro. 2017;4. doi:10.1523/ENEURO.0339-16.2017

915 41. Nicolson T. The genetics of hair-cell function in zebrafish. J Neurogenet. 2017;31: 102–112.
916 doi:10.1080/01677063.2017.1342246

917 42. Mo W, Chen F, Nechiporuk A, Nicolson T. Quantification of vestibular-induced eye
918 movements in zebrafish larvae. BMC Neurosci. 2010;11: 110. doi:10.1186/1471-2202-11-
919 110

920 43. Gao Y, Nicolson T. Temporal Vestibular Deficits in synaptojanin 1 (synj1) Mutants. Front Mol
921 Neurosci. 2021;13: 604189. doi:10.3389/fnmol.2020.604189

922 44. Sun P, Zhang Y, Zhao F, Wu J-P, Pun SH, Peng C, et al. An Assay for Systematically
923 Quantifying the Vestibulo-Ocular Reflex to Assess Vestibular Function in Zebrafish Larvae.
924 Front Cell Neurosci. 2018;12: 257. doi:10.3389/fncel.2018.00257

925 45. Tanimoto M, Ota Y, Horikawa K, Oda Y. Auditory input to CNS is acquired coincidentally
926 with development of inner ear after formation of functional afferent pathway in zebrafish.
927 J Neurosci Off J Soc Neurosci. 2009;29: 2762–2767. doi:10.1523/JNEUROSCI.5530-08.2009

928 46. Bianco IH, Ma L-H, Schoppik D, Robson DN, Orger MB, Beck JC, et al. The Tangential Nucleus
929 Controls a Gravito-inertial Vestibulo-ocular Reflex. Curr Biol. 2012;22: 1285–1295.
930 doi:10.1016/j.cub.2012.05.026

931 47. Jia Y, Bagnall MW. Monosynaptic targets of utricular afferents in the larval zebrafish. Front
932 Neurol. 2022;13. doi:10.3389/fneur.2022.937054

933 48. Liu Z, Hildebrand DGC, Morgan JL, Jia Y, Slimmon N, Bagnall MW. Organization of the
934 gravity-sensing system in zebrafish. Nat Commun. 2022;13: 5060. doi:10.1038/s41467-
935 022-32824-w

936 49. Hamling KR, Harmon K, Schoppik D. The Nature and Origin of Synaptic Inputs to
937 Vestibulospinal Neurons in the Larval Zebrafish. eNeuro. 2023;10: ENEURO.0090-23.2023.
938 doi:10.1523/ENEURO.0090-23.2023

939 50. Sugioka T, Tanimoto M, Higashijima S. Biomechanics and neural circuits for vestibular-
940 induced fine postural control in larval zebrafish. Nat Commun. 2023;14: 1217.
941 doi:10.1038/s41467-023-36682-y

942 51. Muto A, Ohkura M, Abe G, Nakai J, Kawakami K. Real-Time Visualization of Neuronal
943 Activity during Perception. Curr Biol. 2013;23: 307–311. doi:10.1016/j.cub.2012.12.040

944 52. Privat M, Romano SA, Pietri T, Jouary A, Boulanger-Weill J, Elbaz N, et al. Sensorimotor
945 Transformations in the Zebrafish Auditory System. Curr Biol. 2019;29: 4010-4023.e4.
946 doi:10.1016/j.cub.2019.10.020

947 53. Tanimoto M, Watakabe I, Higashijima S. Tiltable objective microscope visualizes selectivity
948 for head motion direction and dynamics in zebrafish vestibular system. Nat Commun.
949 2022;13: 7622. doi:10.1038/s41467-022-35190-9

950 54. Kohashi T, Oda Y. Initiation of Mauthner- or Non-Mauthner-Mediated Fast Escape Evoked
951 by Different Modes of Sensory Input. J Neurosci. 2008;28: 10641–10653.
952 doi:10.1523/JNEUROSCI.1435-08.2008

953 55. Sillar KT. Escape Behaviour: Reciprocal Inhibition Ensures Effective Escape Trajectory. Curr
954 Biol. 2009;19: R697–R699. doi:10.1016/j.cub.2009.07.015

955 56. López-Schier H. Neuroplasticity in the acoustic startle reflex in larval zebrafish. Curr Opin
956 Neurobiol. 2019;54: 134–139. doi:10.1016/j.conb.2018.10.004

957 57. Vanwalleghem G, Heap LA, Scott EK. A profile of auditory-responsive neurons in the larval
958 zebrafish brain. J Comp Neurol. 2017;525: 3031–3043. doi:10.1002/cne.24258

959 58. Inoue M, Tanimoto M, Oda Y. The role of ear stone size in hair cell acoustic sensory
960 transduction. Sci Rep. 2013;3: 2114. doi:10.1038/srep02114

961 59. Echteler SM. Connections of the auditory midbrain in a teleost fish, Cyprinus carpio. J Comp
962 Neurol. 1984;230: 536–551. doi:10.1002/cne.902300405

963 60. Edds-Walton PL, Fay RR. Directional and frequency response characteristics in the
964 descending octaval nucleus of the toadfish (Opsanus tau). J Comp Physiol A. 2008;194:
965 1013–1029. doi:10.1007/s00359-008-0373-8

966 61. McCormick CA. Anatomy of the Central Auditory Pathways of Fish and Amphibians. In: Fay
967 RR, Popper AN, editors. Comparative Hearing: Fish and Amphibians. New York, NY:
968 Springer; 1999. pp. 155–217. doi:10.1007/978-1-4612-0533-3_5

969 62. Marsden KC, Granato M. In vivo Ca2+ imaging reveals that decreased dendritic excitability
970 drives startle habituation. Cell Rep. 2015;13: 1733–1740. doi:10.1016/j.celrep.2015.10.060

971 63. Xu L, Guan NN, Huang C-X, Hua Y, Song J. A neuronal circuit that generates the temporal
972 motor sequence for the defensive response in zebrafish larvae. Curr Biol. 2021;31: 3343-
973 3357.e4. doi:10.1016/j.cub.2021.06.054

974 64. Shimazaki T, Tanimoto M, Oda Y, Higashijima S. Behavioral Role of the Reciprocal Inhibition
975 between a Pair of Mauthner Cells during Fast Escapes in Zebrafish. J Neurosci. 2019;39:
976 1182–1194. doi:10.1523/JNEUROSCI.1964-18.2018

977 65. Koyama M, Kinkhabwala A, Satou C, Higashijima S, Fetcho J. Mapping a sensory-motor
978 network onto a structural and functional ground plan in the hindbrain. Proc Natl Acad Sci.
979 2011;108: 1170–1175. doi:10.1073/pnas.1012189108

980 66. Thiele TR, Donovan JC, Baier H. Descending Control of Swim Posture by a Midbrain Nucleus
981 in Zebrafish. Neuron. 2014;83: 679–691. doi:10.1016/j.neuron.2014.04.018

982 67. Migault G, van der Plas TL, Trentesaux H, Panier T, Candelier R, Proville R, et al. Whole-Brain
983 Calcium Imaging during Physiological Vestibular Stimulation in Larval Zebrafish. Curr Biol.
984 2018;28: 3723-3735.e6. doi:10.1016/j.cub.2018.10.017

985 68. Severi KE, Portugues R, Marques JC, O'Malley DM, Orger MB, Engert F. Neural Control and
986 Modulation of Swimming Speed in the Larval Zebrafish. Neuron. 2014;83: 692–707.
987 doi:10.1016/j.neuron.2014.06.032

988 69. Wang W-C, McLean DL. Selective Responses to Tonic Descending Commands by Temporal
989 Summation in a Spinal Motor Pool. Neuron. 2014;83: 708–721.
990 doi:10.1016/j.neuron.2014.06.021

991 70. Sankrithi NS, O'Malley DM. Activation of a multisensory, multifunctional nucleus in the
992 zebrafish midbrain during diverse locomotor behaviors. Neuroscience. 2010;166: 970–993.
993 doi:10.1016/j.neuroscience.2010.01.003

994 71. Berg EM, Mrowka L, Bertuzzi M, Madrid D, Picton LD, El Manira A. Brainstem circuits
995 encoding start, speed, and duration of swimming in adult zebrafish. Neuron. 2023;111:
996 372-386.e4. doi:10.1016/j.neuron.2022.10.034

997 72. Leung LC, Wang GX, Madelaine R, Skariah G, Kawakami K, Deisseroth K, et al. Neural
998 signatures of sleep in zebrafish. Nature. 2019;571: 198–204. doi:10.1038/s41586-019-
999 1336-7

1000 73. Schöneberg J, Pavlin MR, Yan S, Righini M, Lee I-H, Carlson L-A, et al. ATP-dependent force
1001 generation and membrane scission by ESCRT-III and Vps4. Science. 2018;362: 1423–1428.
1002 doi:10.1126/science.aat1839

1003 74. Su M, Guo EZ, Ding X, Li Y, Tarrasch JT, Brooks CL, et al. Mechanism of Vps4 hexamer
1004 function revealed by cryo-EM. Sci Adv. 2017;3: e1700325. doi:10.1126/sciadv.1700325

1005 75. Babst M, Davies BA, Katzmann DJ. Regulation of Vps4 during MVB sorting and cytokinesis.
1006 Traffic Cph Den. 2011;12: 1298–1305. doi:10.1111/j.1600-0854.2011.01230.x

1007 76. Piper RC, Katzmann DJ. Biogenesis and Function of Multivesicular Bodies. Annu Rev Cell Dev
1008 Biol. 2007;23: 519–547. doi:10.1146/annurev.cellbio.23.090506.123319

1009 77. Bebelman MP, Janssen E, Pegtel DM, Crudden C. The forces driving cancer extracellular
1010 vesicle secretion. Neoplasia N Y N. 2020;23: 149–157. doi:10.1016/j.neo.2020.11.011

1011 78. Meldolesi J. Exosomes and Ectosomes in Intercellular Communication. Curr Biol. 2018;28:
1012 R435–R444. doi:10.1016/j.cub.2018.01.059

1013 79. Dobrowolski R, De Robertis EM. Endocytic control of growth factor signalling: multivesicular
1014 bodies as signalling organelles. Nat Rev Mol Cell Biol. 2012;13: 53–60.
1015 doi:10.1038/nrm3244

1016 80. Palmulli R, van Niel G. To be or not to be... secreted as exosomes, a balance finely tuned by
1017 the mechanisms of biogenesis. Stahl P, Raposo G, editors. Essays Biochem. 2018;62: 177–
1018 191. doi:10.1042/EBC20170076

1019 81. Cocucci E, Racchetti G, Meldolesi J. Shedding microvesicles: artefacts no more. Trends Cell
1020 Biol. 2009;19: 43–51. doi:10.1016/j.tcb.2008.11.003

1021 82. Raymond CK, Howald-Stevenson I, Vater CA, Stevens TH. Morphological classification of the
1022 yeast vacuolar protein sorting mutants: evidence for a prevacuolar compartment in class E
1023 vps mutants. Mol Biol Cell. 1992;3: 1389–1402. doi:10.1091/mbc.3.12.1389

1024 83. Frankel E, Shankar R, Moresco J, Yates J, Volkmann N, Audhya A. Ist1 regulates ESCRT-III
1025 assembly and function during multivesicular endosome biogenesis in Caenorhabditis
1026 elegans embryos. Nat Commun. 2017;8. doi:10.1038/s41467-017-01636-8

1027 84. Bishop N, Woodman P. ATPase-defective Mammalian VPS4 Localizes to Aberrant
1028 Endosomes and Impairs Cholesterol Trafficking. Mol Biol Cell. 2000;11: 227–239.

1029 85. González AE, Muñoz VC, Cavieres VA, Bustamante HA, Cornejo V-H, Januário YC, et al.
1030 Autophagosomes cooperate in the degradation of intracellular C-terminal fragments of
1031 the amyloid precursor protein via the MVB/lysosomal pathway. FASEB J. 2017;31: 2446–
1032 2459. doi:10.1096/fj.201600713R

1033 86. Willén K, Edgar JR, Hasegawa T, Tanaka N, Futter CE, Gouras GK. Aβ accumulation causes
1034 MVB enlargement and is modelled by dominant negative VPS4A. Mol Neurodegener.
1035 2017;12: 61. doi:10.1186/s13024-017-0203-y

1036 87. Zhang Y, Liu Y, Liu H, Tang WH. Exosomes: biogenesis, biologic function and clinical
1037 potential. Cell Biosci. 2019;9: 19. doi:10.1186/s13578-019-0282-2

1038 88. Waqas MY, Javid MA, Nazir MM, Niaz N, Nisar MF, Manzoor Z, et al. Extracellular vesicles
1039 and exosome: insight from physiological regulatory perspectives. J Physiol Biochem.
1040 2022;78: 573–580. doi:10.1007/s13105-022-00877-6

1041 89. Colombo M, Raposo G, Théry C. Biogenesis, Secretion, and Intercellular Interactions of
1042 Exosomes and Other Extracellular Vesicles. Annu Rev Cell Dev Biol. 2014;30: 255–289.
1043 doi:10.1146/annurev-cellbio-101512-122326

1044 90. Gurunathan S, Kang M-H, Kim J-H. A Comprehensive Review on Factors Influences
1045 Biogenesis, Functions, Therapeutic and Clinical Implications of Exosomes. Int J
1046 Nanomedicine. 2021;16: 1281–1312. doi:10.2147/IJN.S291956

1047 91. Han W, Zhang H, Feng L, Dang R, Wang J, Cui C, et al. The emerging role of exosomes in
1048 communication between the periphery and the central nervous system. MedComm.
1049 2023;4: e410. doi:10.1002/mco2.410

1050 92. Duarte-Silva E, Oriá AC, Mendonça IP, de Melo MG, Paiva IHR, Maes M, et al. Tiny in size,
1051 big in impact: Extracellular vesicles as modulators of mood, anxiety and
1052 neurodevelopmental disorders. Neurosci Biobehav Rev. 2022;135: 104582.
1053 doi:10.1016/j.neubiorev.2022.104582

1054 93. Dilsiz N. Role of exosomes and exosomal microRNAs in cancer. Future Sci OA. 2020;6:
1055 FSO465. doi:10.2144/fsoa-2019-0116

1056 94. Gomes AR, Sangani NB, Fernandes TG, Diogo MM, Curfs LMG, Reutelingsperger CP.
1057 Extracellular Vesicles in CNS Developmental Disorders. Int J Mol Sci. 2020;21: 9428.
1058 doi:10.3390/ijms21249428

1059 95. Lim Y-J, Lee S-J. Are exosomes the vehicle for protein aggregate propagation in
1060 neurodegenerative diseases? Acta Neuropathol Commun. 2017;5: 64.
1061 doi:10.1186/s40478-017-0467-z

1062 96. Budnik V, Ruiz-Cañada C, Wendler F. Extracellular vesicles round off communication in the
1063 nervous system. Nat Rev Neurosci. 2016;17: 160–172. doi:10.1038/nrn.2015.29

1064 97. Gurung S, Perocheau D, Touramanidou L, Baruteau J. The exosome journey: from
1065 biogenesis to uptake and intracellular signalling. Cell Commun Signal CCS. 2021;19: 47.
1066 doi:10.1186/s12964-021-00730-1

1067 98. Hamling KR, Harmon K, Kimura Y, Higashijima S, Schoppik D. The vestibulospinal nucleus is a
1068 locus of balance development. bioRxiv. 2023; 2023.12.06.570482.
1069 doi:10.1101/2023.12.06.570482

1070 99. Lacoste AMB, Schoppik D, Robson DN, Haesemeyer M, Portugues R, Li JM, et al. A
1071 convergent and essential interneuron pathway for Mauthner-cell-mediated escapes. Curr
1072 Biol CB. 2015;25: 1526–1534. doi:10.1016/j.cub.2015.04.025

1073 100. Fukushima K. The interstitial nucleus of Cajal and its role in the control of movements of
1074 head and eyes. Prog Neurobiol. 1987;29: 107–192. doi:10.1016/0301-0082(87)90016-5

1075 101. Matsuda K, Kubo F. Circuit Organization Underlying Optic Flow Processing in Zebrafish.
1076 Front Neural Circuits. 2021;15. Available:
1077 https://www.frontiersin.org/articles/10.3389/fncir.2021.709048

1078 102. Liu Z, Bagnall MW. Organization of vestibular circuits for postural control in zebrafish. Curr
1079 Opin Neurobiol. 2023;82: 102776. doi:10.1016/j.conb.2023.102776

1080 103. Huda MN, Nafiujjaman M, Deaguero IG, Okonkwo J, Hill ML, Kim T, et al. Potential use of
1081 exosomes as diagnostic biomarker and in targeted drug delivery: progress in clinical and
1082 preclinical application. ACS Biomater Sci Eng. 2021;7: 2106–2149.
1083 doi:10.1021/acsbiomaterials.1c00217

1084 104. Chen Y, Li J, Ma B, Li N, Wang S, Sun Z, et al. MSC-derived exosomes promote recovery
1085 from traumatic brain injury via microglia/macrophages in rat. Aging. 2020;12: 18274–
1086 18296. doi:10.18632/aging.103692

1087 105. Yari H, Mikhailova MV, Mardasi M, Jafarzadehgharehziaaddin M, Shahrokh S, Thangavelu
1088 L, et al. Emerging role of mesenchymal stromal cells (MSCs)-derived exosome in
1089 neurodegeneration-associated conditions: a groundbreaking cell-free approach. Stem Cell
1090 Res Ther. 2022;13: 423. doi:10.1186/s13287-022-03122-5

1091 106. Zhang X, Jiang W, Lu Y, Mao T, Gu Y, Ju D, et al. Exosomes combined with biomaterials in
1092 the treatment of spinal cord injury. Front Bioeng Biotechnol. 2023;11: 1077825.
1093 doi:10.3389/fbioe.2023.1077825

1094 107. Westerfield M. The Zebrafish Book. A Guide for the Laboratory Use of Zebrafish (Danio
1095 rerio), 4th Edition. University of Oregon Press; 2000.

1096 108. Knapik EW, Goodman A, Ekker M, Chevrette M, Delgado J, Neuhauss S, et al. A
1097 microsatellite genetic linkage map for zebrafish (Danio rerio). Nat Genet. 1998;18: 338–
1098 343. doi:10.1038/ng0498-338

1099 109. Erickson T, Morgan CP, Olt J, Hardy K, Busch-Nentwich E, Maeda R, et al. Integration of
1100 Tmc1/2 into the mechanotransduction complex in zebrafish hair cells is regulated by
1101 Transmembrane O-methyltransferase (Tomt). Ginty DD, editor. eLife. 2017;6: e28474.
1102 doi:10.7554/eLife.28474

1103 110. Smith ET, Pacentine I, Shipman A, Hill M, Nicolson T. Disruption of tmc1/2a/2b Genes in
1104 Zebrafish Reveals Subunit Requirements in Subtypes of Inner Ear Hair Cells. J Neurosci.
1105 2020;40: 4457–4468. doi:10.1523/JNEUROSCI.0163-20.2020

1106 111. Mirat O, Sternberg JR, Severi KE, Wyart C. ZebraZoom: an automated program for high-
1107 throughput behavioral analysis and categorization. Front Neural Circuits. 2013;7: 107.
1108 doi:10.3389/fncir.2013.00107

1109 112. Budick SA, O'Malley DM. Locomotor repertoire of the larval zebrafish: swimming, turning
1110 and prey capture. J Exp Biol. 2000;203: 2565–2579. doi:10.1242/jeb.203.17.2565

1111 113. Makhankov YV, Rinner O, Neuhauss SCF. An inexpensive device for non-invasive
1112 electroretinography in small aquatic vertebrates. J Neurosci Methods. 2004;135: 205–210.
1113 doi:10.1016/j.jneumeth.2003.12.015

1114 114. Verweij FJ, Revenu C, Arras G, Dingli F, Loew D, Pegtel DM, et al. Live Tracking of Inter-
1115 organ Communication by Endogenous Exosomes In Vivo. Dev Cell. 2019;48: 573-589.e4.
1116 doi:10.1016/j.devcel.2019.01.004

1117 115. Kim D, Pertea G, Trapnell C, Pimentel H, Kelley R, Salzberg SL. TopHat2: accurate alignment
1118 of transcriptomes in the presence of insertions, deletions and gene fusions. Genome Biol.
1119 2013;14: R36. doi:10.1186/gb-2013-14-4-r36

1120 116. Afgan E, Baker D, van den Beek M, Blankenberg D, Bouvier D, Čech M, et al. The Galaxy
1121 platform for accessible, reproducible and collaborative biomedical analyses: 2016 update.
1122 Nucleic Acids Res. 2016;44: W3–W10. doi:10.1093/nar/gkw343

1123 117. Gahtan E, Sankrithi N, Campos JB, O'Malley DM. Evidence for a widespread brain stem
1124 escape network in larval zebrafish. J Neurophysiol. 2002;87: 608–614.
1125 doi:10.1152/jn.00596.2001

1126 118. Wehner D, Becker T, Becker CG. Restoration of anatomical continuity after spinal cord
1127 transection depends on Wnt/β-catenin signaling in larval zebrafish. Data Brief. 2017;16:
1128 65–70. doi:10.1016/j.dib.2017.10.068

1129 119. Sehnal D, Bittrich S, Deshpande M, Svobodová R, Berka K, Bazgier V, et al. Mol* Viewer:
1130 modern web app for 3D visualization and analysis of large biomolecular structures. Nucleic
1131 Acids Res. 2021;49: W431–W437. doi:10.1093/nar/gkab314

1132

1133

1134 FIGURE LEGENDS

1135

1136 **Figure 1. The T248I mutation in *vps4a* reduces ATPase activity and ESCRT-III filament**
1137 **disassembly. A,** *vps4a* is located on Chromosome 25 in a location corresponding to where
1138 classical mapping methods have identified the location of the gene responsible for the
1139 *raumschiff* phenotypes. **B,** Bar diagram of Vps4a protein showing the location of the T248I
1140 mutation. **C,** Atomic model structure of the $Vps4^{E233Q}$ hexamer, with T248 marked in magenta
1141 (Image adapted from the RCSB PDB ID:5XMI, using Mol*). **D,** Mutant Vps4 (T254I) yeast
1142 protein has decreased ATP activity compared to wild-type Vps4 protein. **E,** Sedimentation
1143 analysis of Vps4 and Vps4(T254I)-mediated disassembly of ESCRT-III filaments. Pellet (P) and
1144 supernatant (S) fractions were analyzed by SDS-PAGE. Marker (M). **F,** Negative staining EM
1145 micrograph of sedimentation analysis of ESCRT-III filament disassembly.

1146

1147 **Figure 2. *vps4a^{T248I}* mutants have enlarged endosomal compartments in the CNS. A,**
1148 Confocal Z-projections of a 5 dpf wild-type zebrafish larva labeled with HCR RNA-FISH probes
1149 for *vps4a.* fb, forebrain; ot, optic tectum; tpz, tectal proliferation zone, cb, cerebellum; hb,

1150 hindbrain. **B,** LysoTracker staining of 5 dpf wild-type siblings and *vps4a*^{T248I} mutants show an
1151 increased staining in the mutant. **C,** Acidic membrane compartment size in the hindbrain of
1152 *vps4a*^{T248I} mutants (N = 10) is significantly larger than those in wild-type siblings (N = 7).
1153 LysoTracker vital dye taken up by *vps4a*^{T248I} mutants (N = 10), measured as normalized pixel
1154 integrated density, is significantly higher compared to wild-type siblings (N =7).
1155
1156 **Figure 3. *vps4a*^{T248I} mutants release fewer exosomes. A,** Schematic of injecting 1-cell stage
1157 nacre-background embryos with pUbi:CD63-pHluorin. Healthy larvae were sorted on 1 dpf, and
1158 larvae expressing CD63-pHluorin in muscle cells was sorted on 3 dpf, for imaging on 4 dpf. **B,**
1159 Decreased CD63-pHluorin expression in 3 dpf *vps4a*^{T248I} mutant CNS blood vessels. **C,** Dorsal
1160 view of 4 dpf zebrafish larva showing the midbrain ventricle. **D,** Decreased CD63-pHluorin
1161 expression in *vps4a*^{T248I} mutant brain ventricles, but trunk muscles express comparable levels to
1162 wild-type siblings. **E,** Pixel intensity of muscles cells is correlated with normalized pixel intensity
1163 of CD63-pHluorin signal in the midbrain ventricle in wild-type siblings (N = 16). **F,** Quantification
1164 of CD63-pHluorin fluorescence in wild-type siblings (N = 16) and *vps4a*^{T248I} mutants (N = 8).
1165
1166 **Figure 4. *vps4a*^{T248I} mutants upregulate stress response and regeneration genes in the**
1167 **CNS. A,** Axons labeled with acetylated tubulin antibody staining of *vps4a*^{T248I} mutants show no
1168 gross morphological defects. Fb, forebrain; ot, optic tectum; mb, midbrain; cb, cerebellum; hb,
1169 hindbrain. **B,** *vps4a*^{T248I} mutants have an increase of morphologically abnormal, pyknotic cells
1170 in the CNS. Two examples are highlighted with black dashed circles. The number of abnormal
1171 cells in the *vps4a*^{T248I} mutants (N = 11) was quantified and found to be significantly higher than
1172 in wild-type siblings (N = 9). **C,** Maximum intensity projections of *atf3* and *jun* mRNA expression
1173 in the hindbrain of 5 dpf wild-type sibling and *vps4a*^{T248I} mutants. **D,** Maximum intensity

1174 projections of *gap43* and *jun* mRNA expression in the hindbrain of 5 dpf wild-type sibling and
1175 *vps4a*^{T248I} mutants.
1176
1177 **Figure 5. Impaired vision in *vps4a*^{T248I} mutants. A,** 5 dpf *vps4a*^{T248I} mutants (N = 10) have a
1178 reduced optomotor response compared to wild-type siblings (N = 12). **B,** Decreased b wave
1179 amplitude in electroretinograms of 5-6 dpf *vps4a*^{T248I} mutants (N = 34) in comparison to wild-
1180 type siblings (N = 23) at brighter light intensities (log -4 to log 0). **C,** HCR RNA-FISH of *gap43*,
1181 *jun* and *opn1sw1* in the eye of *vps4a*^{T248I} mutants compared to wild-type siblings. Pr,
1182 photoreceptors; Rg, retinal ganglion cells, lens.
1183
1184 **Figure 6. *vps4a*^{T248I} mutants have selective defects in vestibular circuitry. A,** 5 dpf
1185 *vps4a*^{T248I} mutants (N = 16) do not have a significantly different VIEM compared to wild-type
1186 siblings (N = 18). **B,** 5 dpf *vps4a*^{T248I} mutants (N = 10) have a reduced VSR compared to wild-
1187 type siblings (N = 7). **C,** Simplified schematic showing the flow of information evoked by head
1188 rotation from the inner ear to hindbrain nuclei, vestibulo-ocular neurons, and motor neurons.
1189 UHC, utricular hair cells; CN VIII, VIIIth nerve; SVN, superior vestibular nucleus; VS,
1190 vestibulospinal cells; TAN, tangential neurons; M, Mauthner cell; CN IV, trochlear nucleus; CN
1191 III, oculomotor nucleus; OM, oculomotor muscles. **D,** 5 dpf larva showing basal GCamP7a
1192 expression and backfill injected Rhodamine-Dextran marking the Mauthner cell. White dotted
1193 lines mark the TAN, SVN and VS. **D'** Pre- and post-stimulus GCaMP7a levels in vestibular
1194 region in a representative wild-type sibling and *vps4a*^{T248I} mutant. The TAN, SVN and VS ROIs
1195 are outlined by dotted lines. **E,** Average trace of normalized fluorescence (F) for the TAN, SVN
1196 and VS of wild-type siblings and *vps4a*^{T248I} mutants during auditory stimulation at 600Hz. **F,**
1197 Percentage change in fluorescence of the TAN, SVN and VS of wild-type siblings and *vps4a*^{T248I}
1198 mutants during auditory stimulation at 600Hz. The VS in *vps4a*^{T248I} mutants (N = 11) have a

1199 reduced change in fluorescence compared to wild-type siblings (N = 15). There is no significant
1200 difference between mutants and wild-type siblings in the TAN or SVN.
1201
1202 **Figure 7. Activation of the ascending auditory pathway in *vps4a^{T248I}* mutants. A,** simplified
1203 schematic showing the flow of information from an auditory stimulus to motor neurons
1204 (responsible for startle reflexes) or to the torus semicircularis (key for auditory processing). S,
1205 saccular otolith; SHC, saccular hair cells; CN VIII, VIIIth nerve; MON, medial octavolateralis
1206 nucleus; M, Mauthner cell; TS, torus semicircularis. **B,** 5 dpf *vps4a^{T248I}* mutants (N = 20) have a
1207 greatly reduced AEBR compared to wild-type siblings (N = 15). **C,** Basal levels of GCaMP7a
1208 expression in the inner ear of 5 dpf larvae, focusing on the saccular hair cells (dotted line) and
1209 statoacoustic ganglion (SAG) (dashed line). **D,** Pre- and post-stimulus GCaMP7a levels in
1210 saccular hair cells and SAG in a representative wild-type sibling and *vps4a^{T248I}* mutant larvae.
1211 **E,** Average traces of normalized fluorescence (F) for the saccular hair cells and SAG of wild-
1212 type siblings and *vps4a^{T248I}* mutants during auditory stimulation at 600Hz. **F,** Percentage
1213 change in fluorescence of the saccular hair cells and SAG of wild-type siblings and *vps4a^{T248I}*
1214 mutants during auditory stimulation at 600Hz. There is no significant difference between
1215 mutants (N = 13) and wild-type siblings (N = 20) in the saccular hair cells or the SAG. **G,**
1216 Representative image of 5 dpf zebrafish basal levels of GCaMP7a expression in the torus
1217 semicircularis (TS). **H,** Pre-and post-stimulus GCaMP7a levels in the TS in representative wild-
1218 type sibling and *vps4a^{T248I}* mutant larvae. **I,** Average trace of normalized fluorescence (F) for
1219 the TS of wild-type siblings and *vps4a^{T248I}* mutants during auditory stimulation at 600Hz. **J,**
1220 There is no significant difference in percentage change fluorescence between *vps4a^{T248I}*
1221 mutants (N = 13) and wild-type siblings (N = 11) in the TS.
1222
1223 **Figure 8. *vps4a^{T248I}* mutants display defects in sensorimotor transformation**. **A,** simplified
1224 schematic showing the flow of information from a tone stimulus from the inner ear to motor

1225 neurons via Mauthner cell and nMLF pathways. S, saccular otolith; SHC, saccular hair cells;
1226 CN VIII, VIIIth nerve; M, Mauthner cell; HB, hindbrain; CRN, cranial relay neurons; nMLF,
1227 nucleus of the medial longitudinal fasciculus. **B,** 7 dpf *vps4a*^{T248I} mutant larvae have an intact
1228 startle reflex when touched. **C,** 7 dpf *vps4a*^{T248I} mutants (N = 11) do not have a significantly
1229 different C-bend angle compared to wild-type siblings (N = 10). **D,** Acetylated tubulin antibody
1230 staining of *vps4a*^{T248I} mutants shows no gross morphological defects in hindbrain/spinal cord or
1231 somatosensory axons. **E,** Representative image of 5 dpf zebrafish, showing location of nMLF
1232 expressing basal levels of GCaMP7a. **F,** Pre- and post-stimulus GCaMP7a levels in the nMLF
1233 in a representative wild-type sibling and *vps4a*^{T248I} mutant. **G,** Average trace of normalized
1234 fluorescence (F) for the nMLF of wild-type siblings and *vps4a*^{T248I} mutants during tone
1235 stimulation at 600Hz. **H,** *vps4a*^{T248I} mutants (N = 11) have a significantly reduced percentage
1236 change fluorescence in the nMLF compared to wild-type siblings (N = 14). **I,** Representative
1237 image of 5 dpf zebrafish trunk showing spinal cord neurons expressing basal levels of
1238 GCaMP7a. **J,** Pre-and post-stimulus GCaMP7a levels in the spinal cord motor neurons of
1239 representative wild-type sibling and *vps4a*^{T248I} mutant. **K,** Average trace of normalized
1240 fluorescence (F) for the spinal cord motor neurons of wild-type siblings and *vps4a*^{T248I} mutants
1241 during tone stimulation at 450Hz. **L,** *vps4a*^{T248I} mutants (N = 9) have a significantly reduced
1242 percentage change fluorescence in spinal cord neurons compared to wild-type siblings (N = 11).
1243
1244 **Figure S1. *vps4a*^{T248I} mutant hair cells do not display changes in LysoTracker labeling or**
1245 **gene expression. A,** Representative maximum projection images of wild-type siblings and
1246 *vps4a*^{T248I} mutant larvae showing LysoTracker staining of saccule and utricle. Hb, hindbrain. **B,**
1247 LysoTracker vital dye taken up by the utricle and saccule of *vps4a*^{T248I} mutants (N = 9),
1248 measured as normalized pixel integrated density, is not significantly higher compared to wild-
1249 type siblings (N =6). **C,** Maximum projection of LysoTracker staining of anterior cristae hair
1250 cells. Anterior cristae hair cells were imaged due to similarity to hair cells and convenience. **D,**

1251 LysoTracker vital dye uptake in apical endosomes in *vps4a*^{T248I} mutant anterior cristae hair cells
1252 (N = 10), measured as normalized pixel integrated density, is not significantly different
1253 compared to wild-type siblings (N = 10). Nuc, nucleus. **E,** Maximum intensity projections of *jun*
1254 mRNA expression in the saccular hair cells and statoacoustic ganglion of 5 dpf wild-type
1255 siblings and *vps4a*^{T248I} mutants.
1256
1257
1258
1259
1260
1261
1262
1263
1264
1265
1266
1267
1268
1269
1270
1271
1272
1273
1274

Fig 1

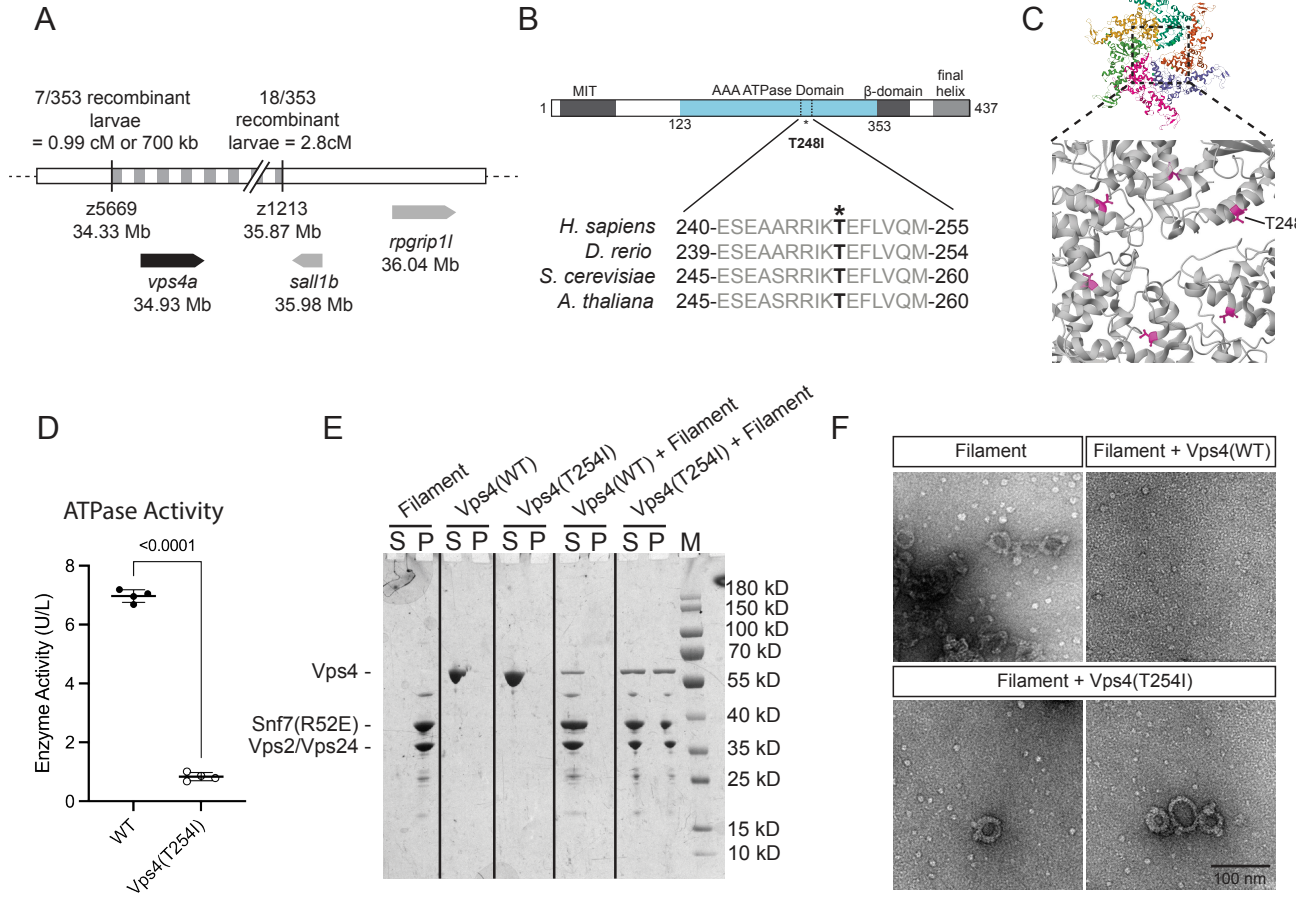
A
7/353 recombinant larvae = 0.99 cM or 700 kb
18/353 recombinant larvae = 2.8cM
z5669
34.33 Mb
z1213
35.87 Mb
rpgrip1l
36.04 Mb
vps4a
34.93 Mb
sall1b
35.98 Mb
B
MIT
AAA ATPase Domain
β-domain
final helix
1
123
353
437
T248I
H. sapiens 240-ESEAARRIKTEFLVQM-255
D. rerio 239-ESEAARRIKTEFLVQM-254
S. cerevisiae 245-ESEASRRIKTEFLVQM-260
A. thaliana 245-ESEASRRIKTEFLVQM-260
C
T248
D
ATPase Activity
<0.0001
Enzyme Activity (U/L)
WT
Vps4(T254I)
E
Filament
Vps4(WT)
Vps4(T254I)
Vps4(WT) + Filament
Vps4(T254I) + Filament
S P S P S P S P S P M
Vps4
Snf7(R52E)
Vps2/Vps24
180 kD
150 kD
100 kD
70 kD
55 kD
40 kD
35 kD
25 kD
15 kD
10 kD
F
Filament
Filament + Vps4(WT)
Filament + Vps4(T254I)
100 nm

Fig 2

A

vps4a expression

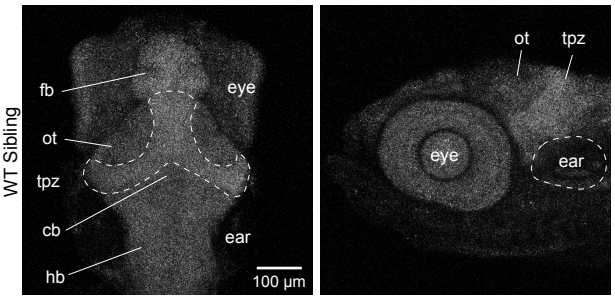

B

LysoTracker Label

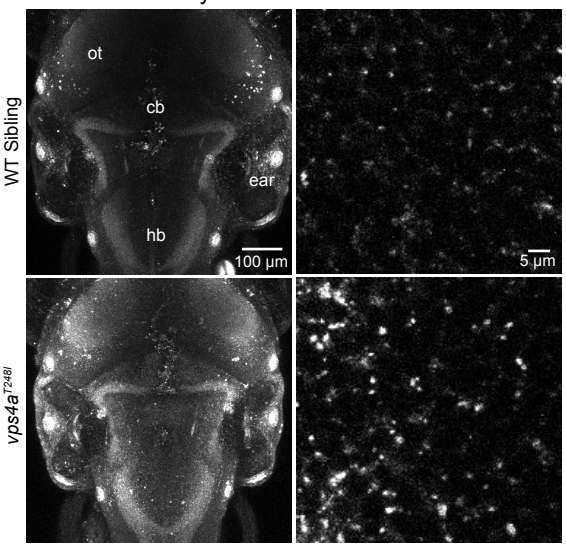

C

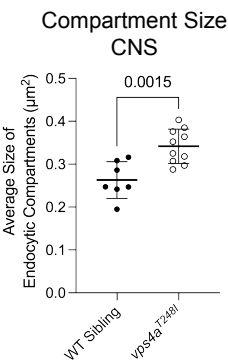

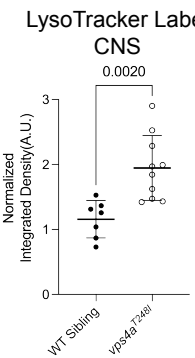

Fig 3

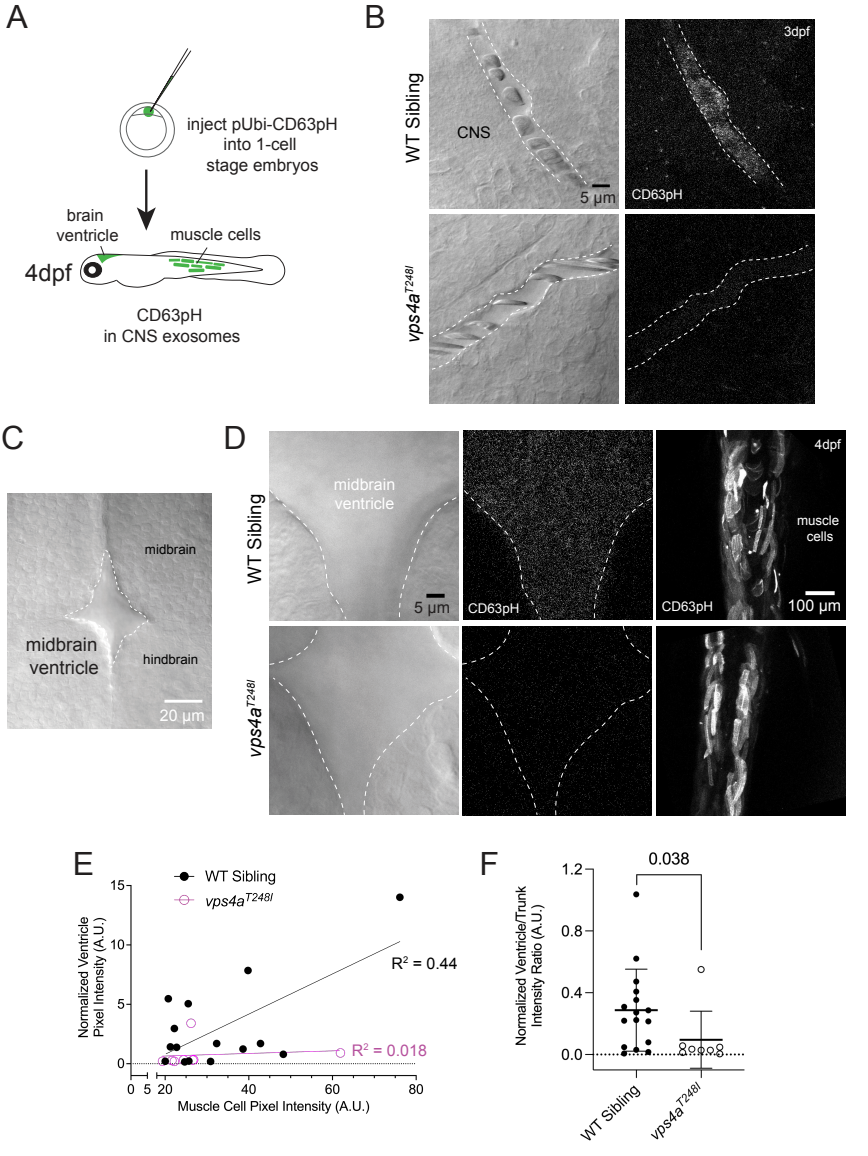
A
inject pUbi-CD63pH
into 1-cell
stage embryos
brain
ventricle
muscle cells
4dpf
CD63pH
in CNS exosomes
B
WT Sibling
CNS
5 µm
3dpf
CD63pH
vps4a T248I
C
midbrain
midbrain
ventricle
hindbrain
20 µm
D
WT Sibling
midbrain
ventricle
5 µm
CD63pH
4dpf
muscle
cells
CD63pH
100 µm
vps4a T248I
E
WT Sibling
vps4a T248I
Normalized Ventricle
Pixel Intensity (A.U.)
R² = 0.44
R² = 0.018
Muscle Cell Pixel Intensity (A.U.)
F
0.038
Normalized Ventricle/Trunk
Intensity Ratio (A.U.)
WT Sibling
vps4a T248I

Fig 4

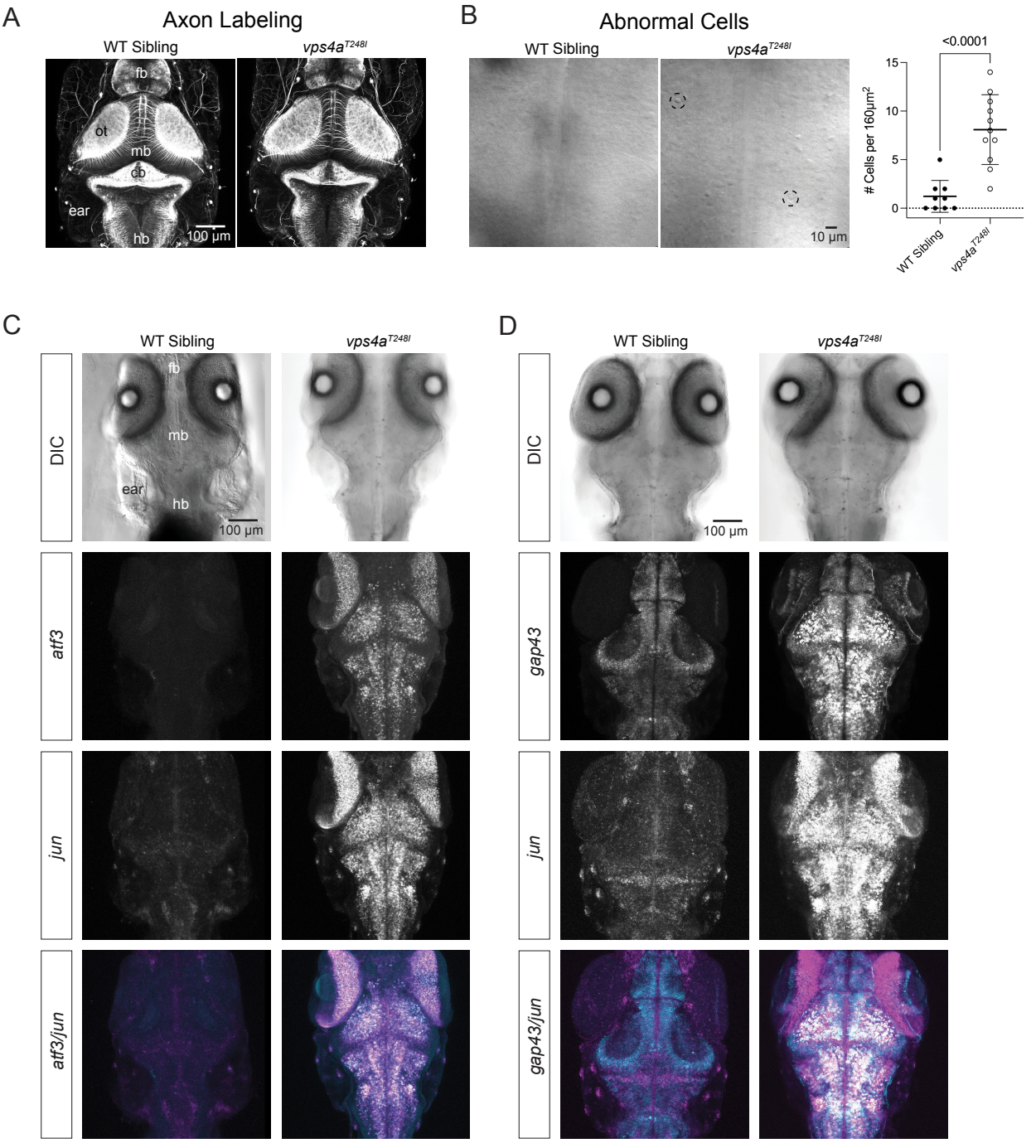
A
Axon Labeling
WT Sibling
vps4a T248I
fb
ot
mb
cb
ear
hb
100 µm
B
Abnormal Cells
WT Sibling
vps4a T248I
10 µm
<0.0001
Cells per 160µm2
15
10
5
0
WT Sibling
vps4a T248I
C
WT Sibling
vps4a T248I
DIC
fb
mb
ear
hb
100 µm
atf3
jun
atf3/jun
D
WT Sibling
vps4a T248I
DIC
100 µm
gap43
jun
gap43/jun

Fig 5

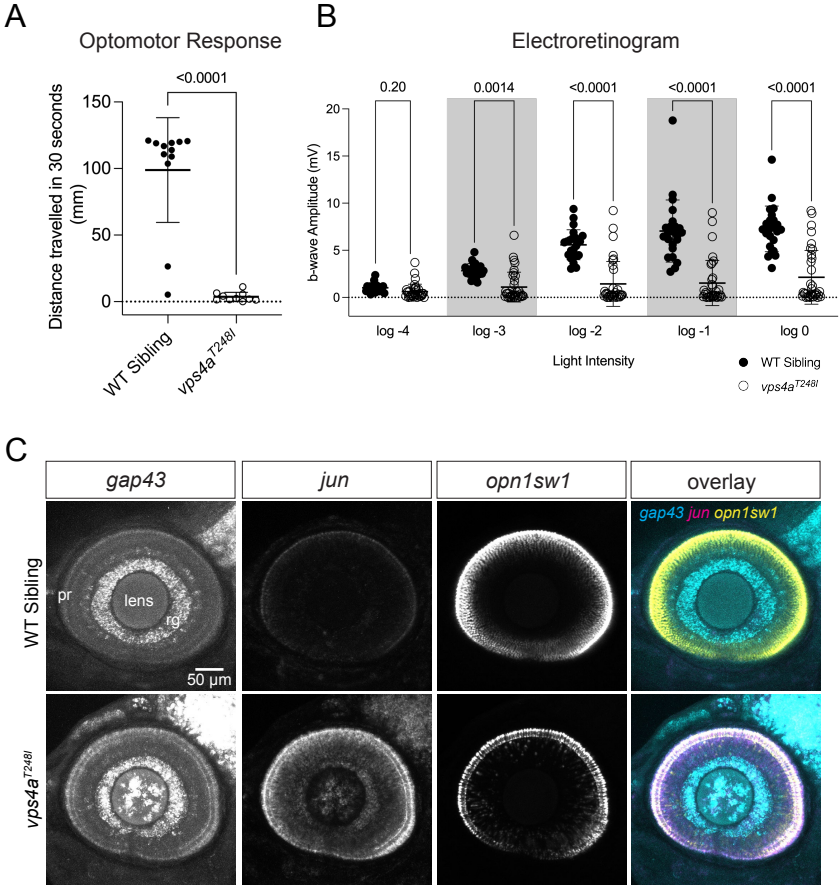
A
Optomotor Response
<0.0001
Distance travelled in 30 seconds (mm)
150
100
50
0
WT Sibling
vps4a T248I
B
Electroretinogram
0.20
0.0014
<0.0001
<0.0001
<0.0001
b-wave Amplitude (mV)
20
15
10
5
0
log -4
log -3
log -2
log -1
log 0
Light Intensity
WT Sibling
vps4a T248I
C
gap43
jun
opn1sw1
overlay
gap43 jun opn1sw1
WT Sibling
vps4a T248I
pr
lens
rg
50 µm

Fig 6

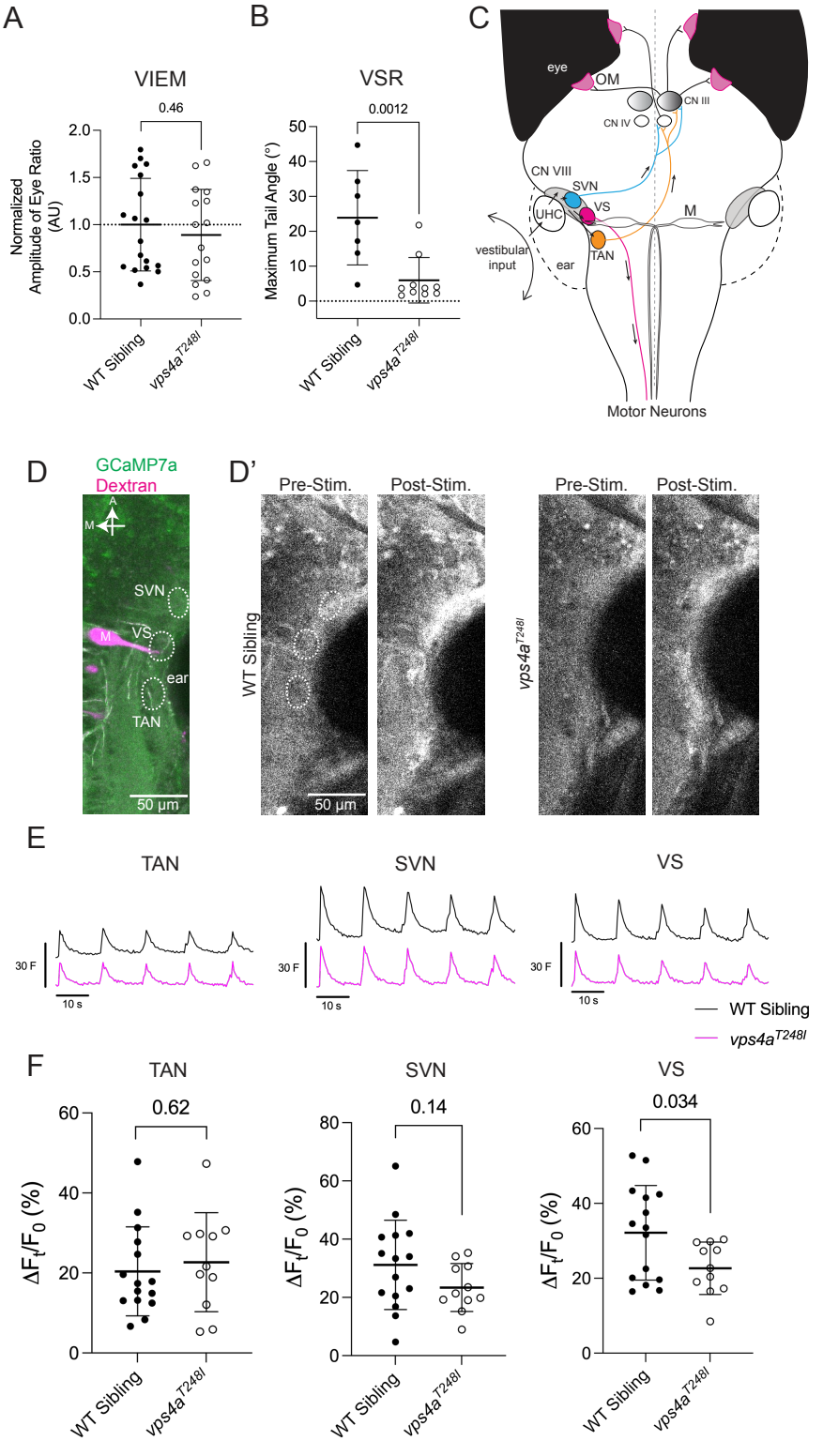
A
VIEM
0.46
Normalized Amplitude of Eye Ratio (AU)
2.0
1.5
1.0
0.5
0.0
WT Sibling
vps4a T248I
B
VSR
0.0012
Maximum Tail Angle (°)
50
40
30
20
10
0
WT Sibling
vps4a T248I
C
eye
OM
CN III
CN IV
CN VIII
SVN
UHC
VS
M
vestibular input
ear
TAN
Motor Neurons
D
GCaMP7a
Dextran
A
M
SVN
VS
M
ear
TAN
50 µm
D'
Pre-Stim.
Post-Stim.
WT Sibling
50 µm
Pre-Stim.
Post-Stim.
vps4a T248I
E
TAN
SVN
VS
30 F
10 s
WT Sibling
vps4a T248I
F
TAN
0.62
SVN
0.14
VS
0.034
ΔFt/F0 (%)
60
40
20
0
80
WT Sibling
vps4a T248I

Fig 7

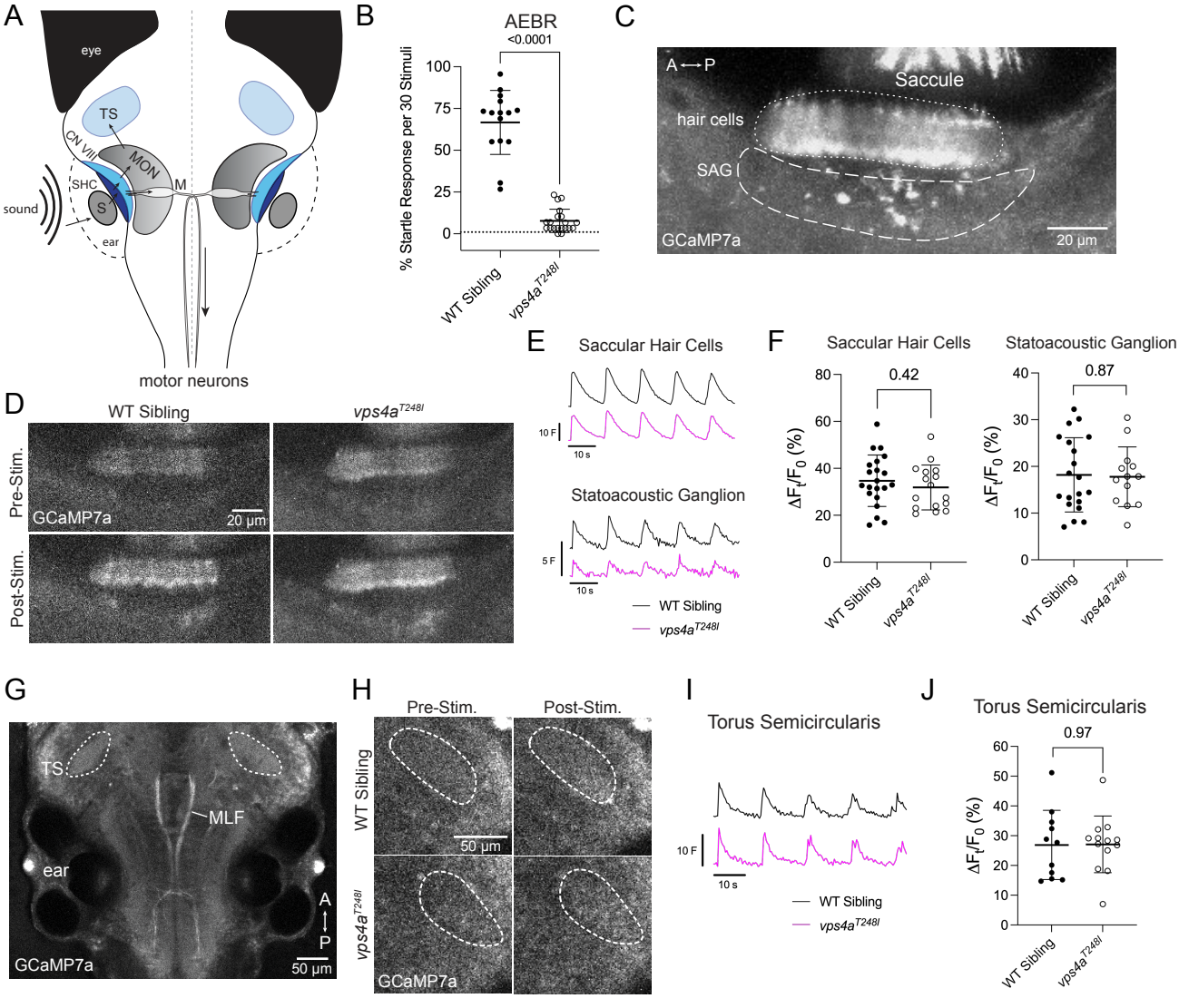
A
eye
TS
CN VIII
MON
SHC
M
S
sound
ear
motor neurons
B
AEBR
<0.0001
% Startle Response per 30 Stimuli
100
75
50
25
0
WT Sibling
vps4a T248I
C
A ⟷ P
Saccule
hair cells
SAG
GCaMP7a
20 µm
D
WT Sibling
vps4a T248I
Pre-Stim.
Post-Stim.
GCaMP7a
20 µm
E
Saccular Hair Cells
10 F
10 s
Statoacoustic Ganglion
5 F
10 s
WT Sibling
vps4a T248I
F
Saccular Hair Cells
0.42
ΔFt/F0 (%)
80
60
40
20
0
WT Sibling
vps4a T248I
Statoacoustic Ganglion
0.87
ΔFt/F0 (%)
40
30
20
10
0
WT Sibling
vps4a T248I
G
TS
MLF
ear
A
P
GCaMP7a
50 µm
H
Pre-Stim.
Post-Stim.
WT Sibling
vps4a T248I
50 µm
GCaMP7a
I
Torus Semicircularis
10 F
10 s
WT Sibling
vps4a T248I
J
Torus Semicircularis
0.97
ΔFt/F0 (%)
60
50
40
30
20
10
0
WT Sibling
vps4a T248I

Fig 8

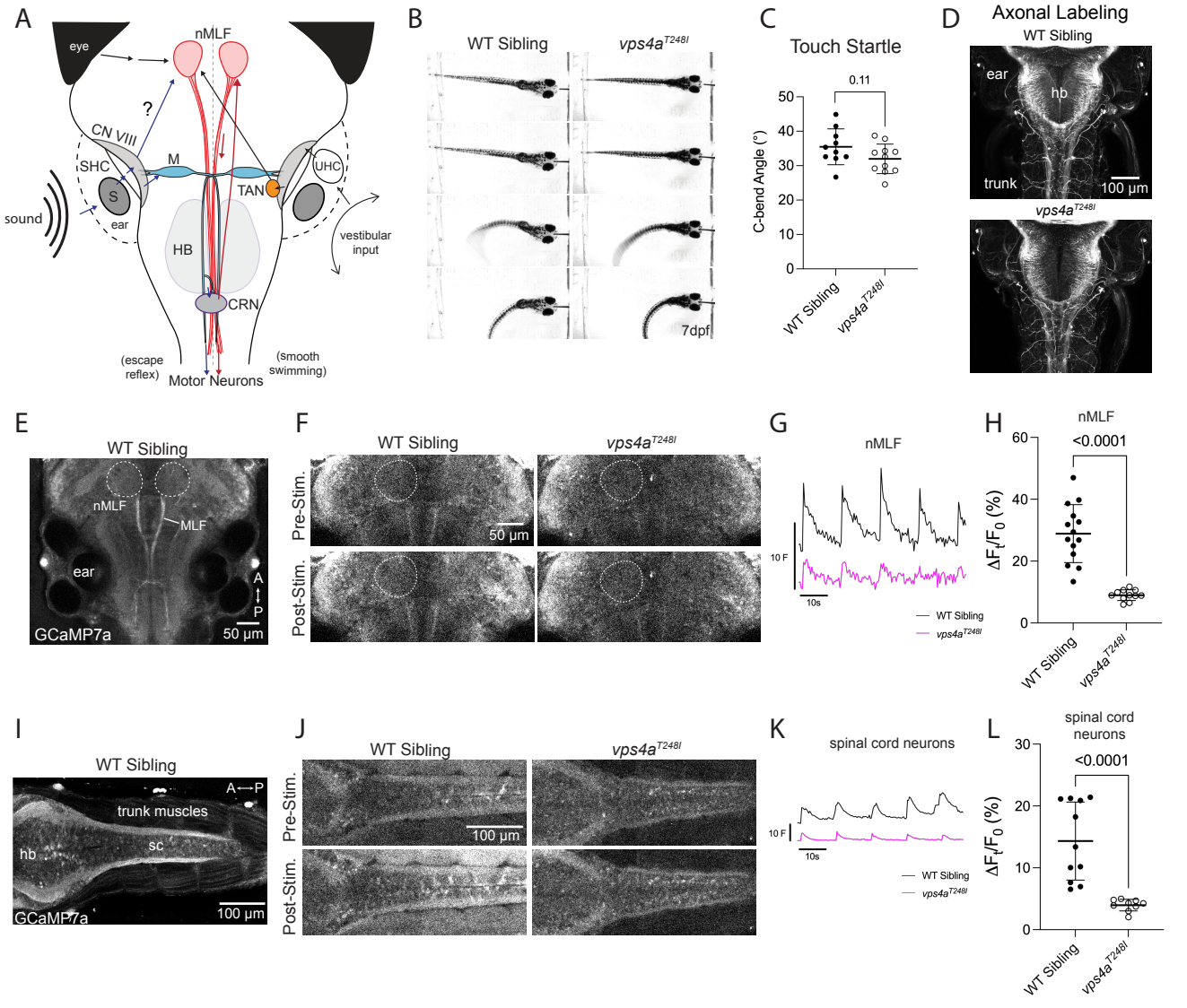
A
eye
nMLF
?
CN VIII
SHC
M
UHC
S
TAN
sound
ear
HB
vestibular input
CRN
(escape reflex)
Motor Neurons
(smooth swimming)
B
WT Sibling
vps4a T248I
7dpf
C
Touch Startle
0.11
C-bend Angle (°)
WT Sibling
vps4a T248I
D
Axonal Labeling
WT Sibling
ear
hb
trunk
100 µm
vps4a T248I
E
WT Sibling
nMLF
MLF
ear
A
P
GCaMP7a
50 µm
F
WT Sibling
vps4a T248I
Pre-Stim.
Post-Stim.
50 µm
G
nMLF
10 F
10s
WT Sibling
vps4a T248I
H
nMLF
<0.0001
ΔFt/F0 (%)
WT Sibling
vps4a T248I
I
WT Sibling
A⟷P
trunk muscles
sc
hb
GCaMP7a
100 µm
J
WT Sibling
vps4a T248I
Pre-Stim.
Post-Stim.
100 µm
K
spinal cord neurons
10 F
10s
WT Sibling
vps4a T248I
L
spinal cord neurons
<0.0001
ΔFt/F0 (%)
WT Sibling
vps4a T248I

Fig S1

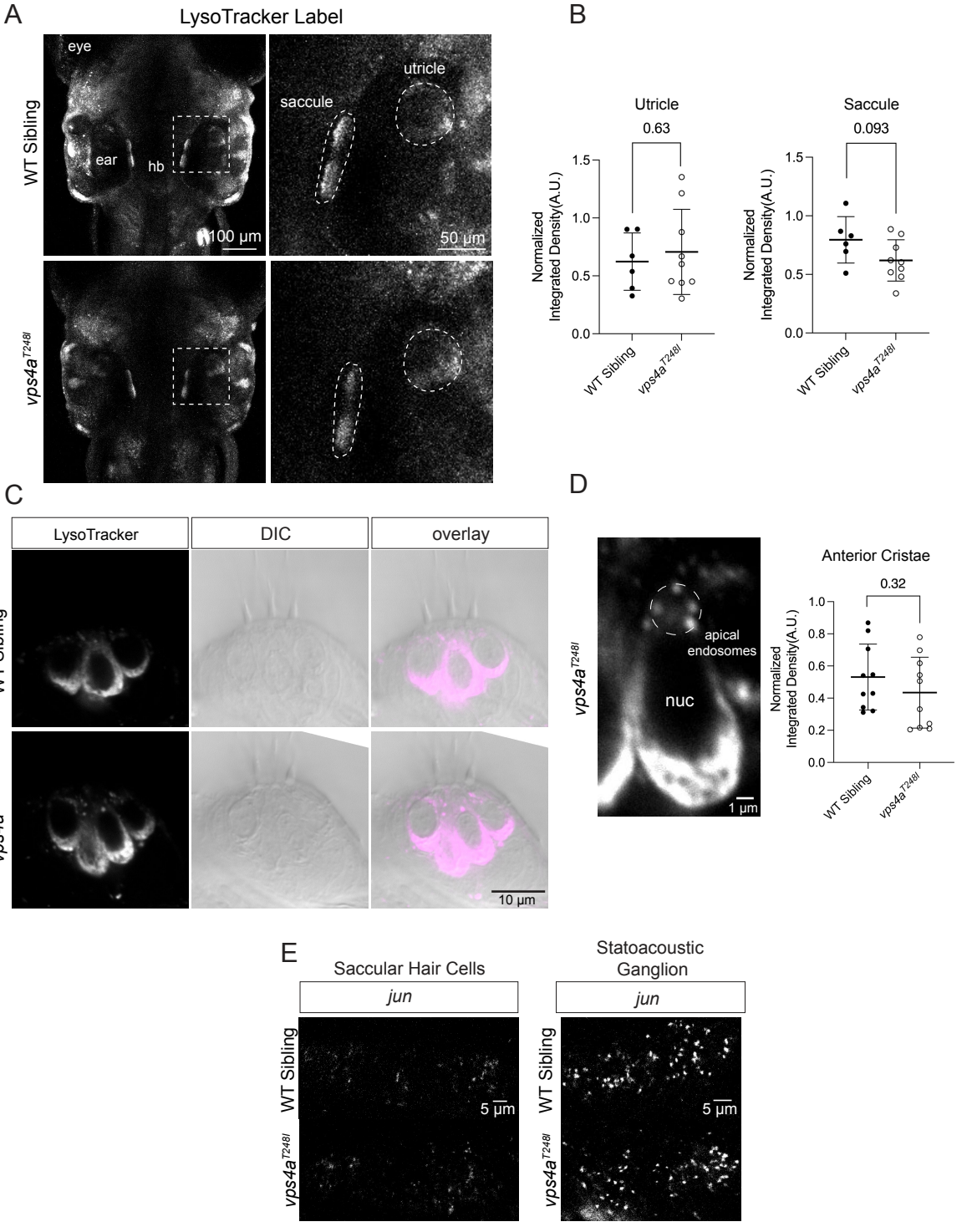
A
LysoTracker Label
eye
ear
hb
100 µm
utricle
saccule
50 µm
WT Sibling
vps4a T248I
B
Utricle
0.63
Saccule
0.093
Normalized Integrated Density(A.U.)
1.5
1.0
0.5
0.0
WT Sibling
vps4a T248I
C
LysoTracker
DIC
overlay
WT Sibling
vps4a T248I
10 µm
D
apical endosomes
nuc
1 µm
Anterior Cristae
0.32
1.0
0.8
0.6
0.4
0.2
0.0
E
Saccular Hair Cells
Statoacoustic Ganglion
jun
5 µm